JOURNAL OF PETROLOGY | VOLUME 55 | NUMBER 11 | PAGES 2155–2192 | 2014 | doi:10.1093/petrology/egu053

High-K Mafic Plinian Eruptions of Volcán de Colima, Mexico

JULIA M. CRUMMY[1]*, IVAN P. SAVOV[2], CARLOS NAVARRO-OCHOA[3], DANIEL J. MORGAN[2] AND MARJORIE WILSON[2]

[1]BRITISH GEOLOGICAL SURVEY, MURCHISON HOUSE, WEST MAINS ROAD, EDINBURGH EH9 3LA, UK

[2]INSTITUTE OF GEOPHYSICS & TECTONICS, SCHOOL OF EARTH & ENVIRONMENT, UNIVERSITY OF LEEDS, LEEDS LS2 9JT, UK

[3]OBSERVATORIO VULCANOLÓGICO DE COLIMA, UNIVERSIDAD DE COLIMA, COLIMA, MEXICO

RECEIVED MARCH 31, 2014; ACCEPTED SEPTEMBER 10, 2014

The last Plinian-type eruption of Volcán de Colima, Mexico, occurred in 1913; this resulted in the removal of the top 100 m of the edifice and the deposition of a tephra layer that blanketed the slopes of the Colima Volcanic Complex (CVC). Road-cuts on the flanks of the nearby Nevado de Colima edifice expose pre-1913 air-fall tephra, pyroclastic flow and ash-rich surge deposits resulting from numerous highly explosive events throughout the Holocene. The majority of the pumice and scoria fallout deposits are medium-K subalkaline basaltic andesite and andesite in composition, defining a clear major element differentiation trend. In contrast, three newly discovered scoria fallout deposits are high-K subalkaline, transitional to alkaline, basaltic andesite in composition and are characterized by the presence of phlogopite; these deposits have high MgO (up to 7·9 wt %), K_2O (up to 2·6 wt %) and P_2O_5 (up to 0·67 wt %) contents. They are also strongly enriched in fluid- and melt-mobile large ion lithophile elements (LILE; Rb, Ba, K, Sr and Th) and light REE (LREE; La, Ce, Pr and Nd) relative to the majority of the Colima tephra fallout deposits. Strontium and Nd isotope systematics reveal that the high-K mafic scoria have more radiogenic Sr ($^{87}Sr/^{86}Sr = 0·70365–0·70408$) and less radiogenic Nd ($^{143}Nd/^{144}Nd = 0·51279–0·51294$) compared with the majority of the subalkaline tephras ($^{87}Sr/^{86}Sr = 0·70338–0·70371$ and $^{143}Nd/^{144}Nd = 0·51290–0·51295$). Two-component mixing models, using whole-rock geochemical data, indicate the importance of magma mixing in the petrogenesis of the Colima magmas, with addition of up to 50% by volume of an alkaline mafic magma component in the most potassic magmas. This is supported by mineral chemistry and textural data, which reveal multiple episodes of decompression and magma mingling within a shallow crustal magma storage region. The presence of these potassic tephra fall deposits among the otherwise prevailing medium-K subalkaline stratigraphy indicates that pulses of K-rich alkaline mafic magmas periodically enter the CVC plumbing system on timescales of a few thousand years and may trigger Plinian explosive eruptions.

KEY WORDS: *tephra; alkaline; Colima; subduction; slab; pyroclastic fall*

INTRODUCTION

Volcán de Colima is the westernmost volcanic centre of the Trans-Mexican Volcanic Belt (TMVB), which is associated with the northeasterly subduction of the young Cocos and Rivera plates under the North American plate (Fig. 1). Volcán de Colima is considered one of North America's most active volcanoes (Cortés *et al.*, 2010; Luhr *et al.*, 2010) and, owing to its relatively good exposure and preserved volcanic record, has been the subject of many petrological, geochemical and geophysical investigations (e.g. Luhr & Carmichael, 1980, 1990*b*; Medina-Martínez, 1983; Robin *et al.*, 1987, 1991; De la Cruz-Reyna, 1993; Luhr, 1993, 2002; Robin & Potrel, 1993; Righter, 2000; Ferrari *et al.*, 2001, 2012; Navarro-Ochoa *et al.*, 2002; Zobin *et al.*, 2002, 2008; Saucedo *et al.*, 2005, 2010; Atlas *et al.*, 2006; Luhr *et al.*,

*Corresponding author. E-mail: juli@bgs.ac.uk

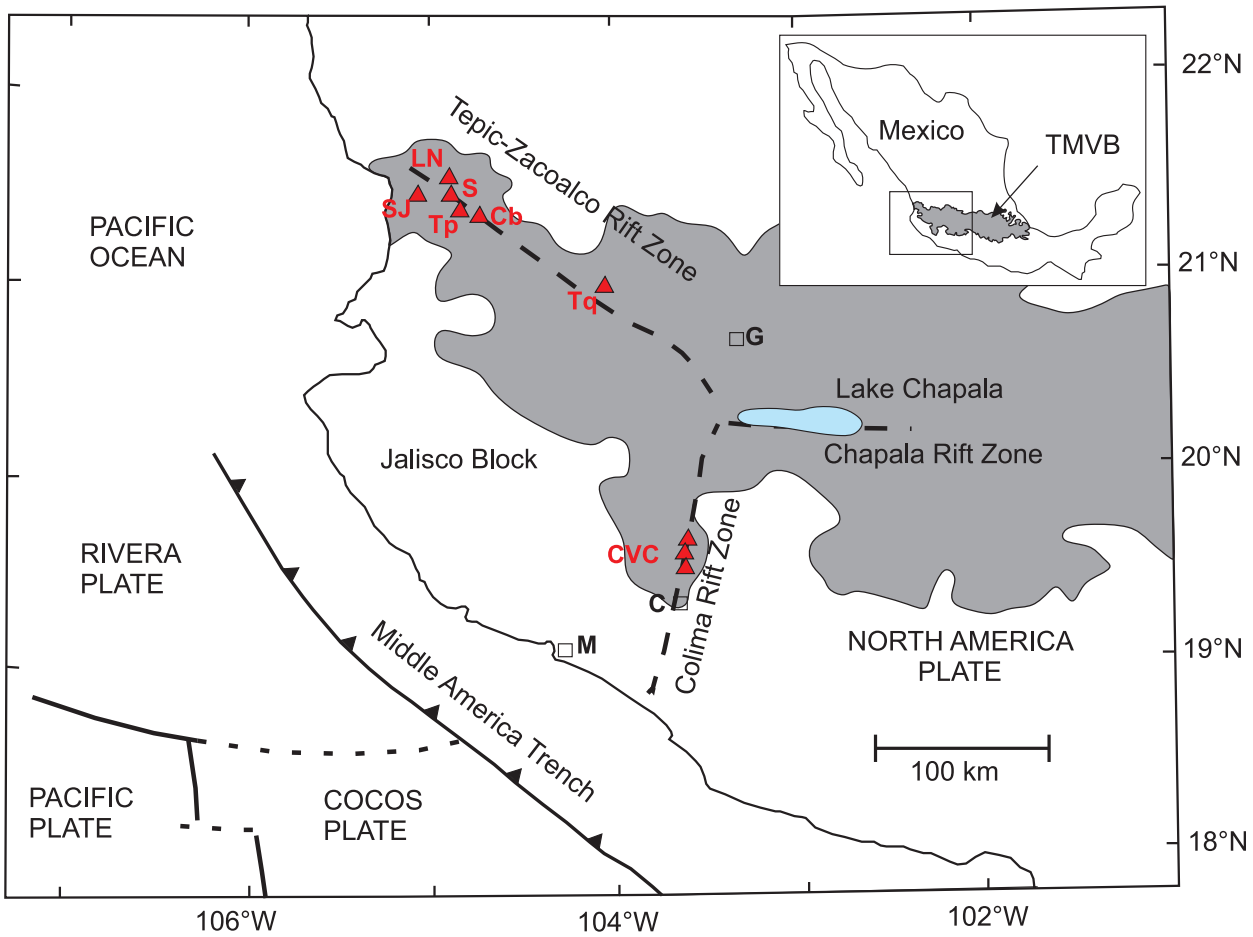

Fig. 1. Location map of the Colima Volcanic Complex (CVC) in the western Trans-Mexican Volcanic Belt (TMVB). Also shown are the Chapala and Tepic–Zacoalco Rift (TZR) Zones. Volcanoes in the TZR: Tq, Volcán Tequila; Cb, Volcán Ceboruco; Tp, Volcán Tepetiltic; S, Volcán Sanganguey; LN, Las Navajas; SJ, Volcán San Juan. Cities: G, Guadalajara; C, Colima; M, Manzanillo.

2006; Valdez-Moreno *et al.*, 2006; Reubi & Blundy, 2008; Savov *et al.*, 2008; Gardine, 2010; Varley *et al.*, 2010).

The current activity of Volcán de Colima is characterized by effusive lava dome growth and blocky lava flows with common (several times daily) small explosions, punctuated by larger Vulcanian-type events producing ash columns rising to 12 km above sea level (Savov *et al.*, 2008; Reubi *et al.*, 2014). However, Volcán de Colima can also produce Plinian-type eruptions. The last such event occurred in 1913, and prior to that in 1818 (Bretón González *et al.*, 2002). Exposed in road-cuts on the slopes of the nearby extinct volcanic edifice of Nevado de Colima are numerous Holocene tephra fallout and surge deposits from such highly explosive eruptions (Fig. 2; Luhr *et al.*, 2010). Radiocarbon dating [183 charcoal dates reported by Luhr *et al.* (2010)] and detailed stratigraphic correlations involving granulometry, petrography and geochemistry reveal that at least 25 Plinian deposits remain preserved, spanning the past 30 kyr (Luhr *et al.*, 2010; Crummy, 2013). During this time period there have also been at least six gravitational collapse events resulting in large debris-avalanche deposits to the south, SE and SW of Volcán de Colima (Robin *et al.*, 1987; Luhr & Prestegaard, 1988; Luhr & Carmichael, 1990*a*; Stoopes & Sheridan, 1992; Komorowski *et al.*, 1997; Cortés *et al.*, 2009; Norini *et al.*, 2010).

In the first study of the Holocene tephra deposits of Volcán de Colima, Luhr & Carmichael (1982) discovered a distinct phlogopite-bearing scoria fallout deposit exposed on the flanks of Nevado de Colima that was clearly different in terms of its geochemistry and mineralogy when compared with the rest of the known deposits, which are medium-K, subalkaline in composition. To explain their observations, those researchers proposed that this tephra resulted from direct mixing between a contemporaneously erupting medium-K subalkaline Colima Volcanic Complex (CVC) magma and a high-K alkaline magma similar in composition to that of nearby alkaline cinder cones on the

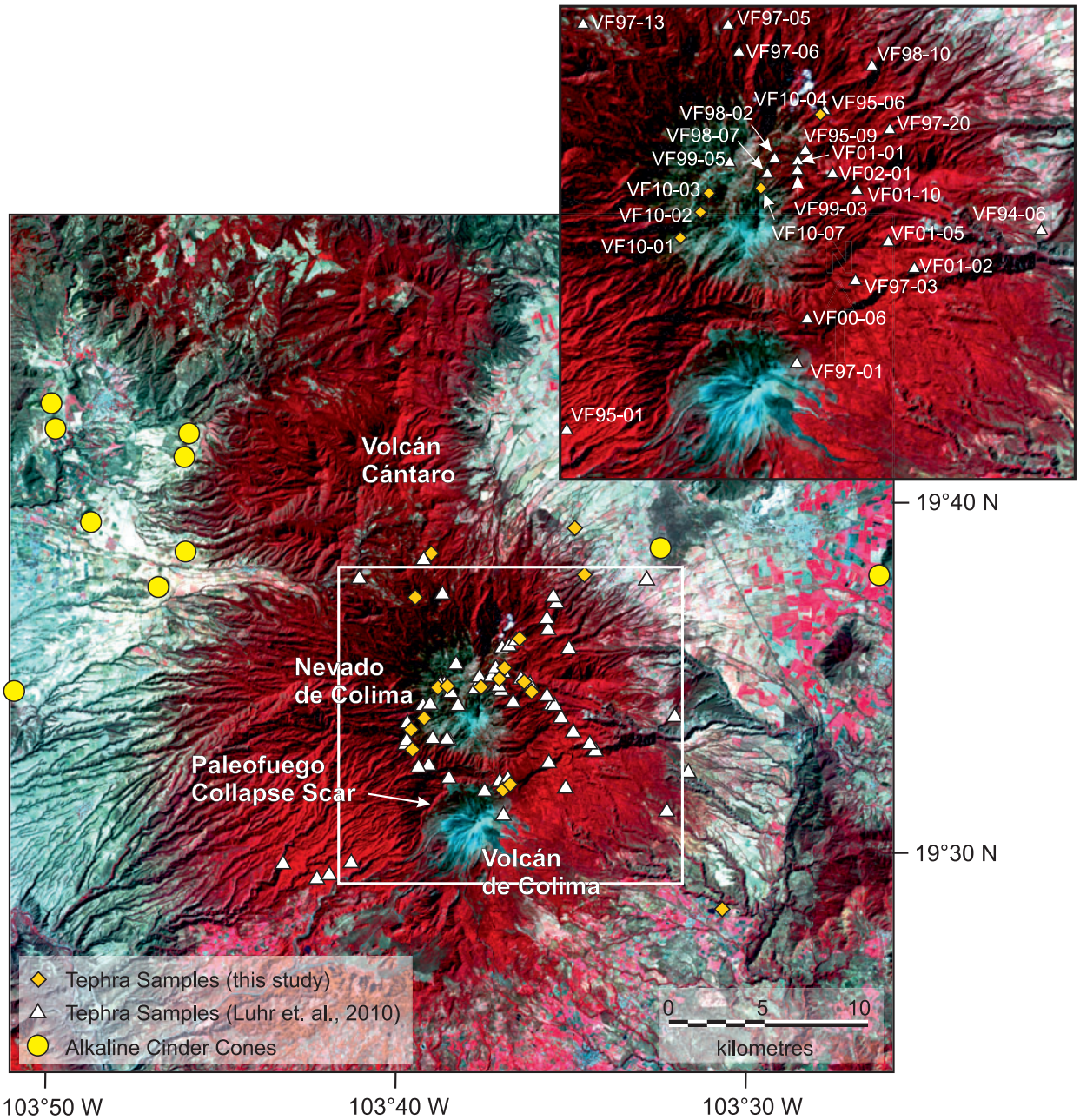

Fig. 2. Detailed map of the CVC showing the southerly trending volcanic chain from Volcán Cántaro in the north to Volcán de Colima in the south. Tephra sample locations from Luhr *et al.* (2010) and this study are shown, as are the locations of the monogenetic alkaline cinder cones (Luhr & Carmichael, 1981; Carmichael *et al.*, 2006). Image is an ASTER image collected from NASA's Terra satellite on 6 February 2003 (NASA's Earth Observatory). Red areas are forested areas, pink areas are farmland and blue areas are unvegetated. Inset map shows the locations of samples used in this study.

flanks of the CVC (Fig. 2); however, this hypothesis was never fully explored. Based on their morphology, the ages of the cinder cones were estimated at 1500 to >20 000 years, coinciding with the explosive eruptions that formed the Holocene CVC stratigraphy (Luhr & Carmichael, 1981). Subsequently, using $^{40}Ar/^{39}Ar$ dating techniques Carmichael *et al.* (2006) dated the alkaline cinder cones, and reported ages of 450–62 ka; these are much older than the proposed mixed tephras that are subject of this study and the study by Luhr & Carmichael (1982).

Through further field, petrological and geochemical studies we have discovered two additional phlogopite-bearing

tephra fallout deposits that are similar to that described by Luhr & Carmichael (1982). Here we present the results of petrological and geochemical investigations of these little known, but distinct, high-K mafic tephras, and explore their relationship with the explosive subalkaline CVC magmas and the high-K alkaline magmas similar to those that erupted through pre-Holocene cinder cones on the valley floor.

GEOLOGICAL SETTING

Volcán de Colima is the youngest, and currently active, volcano of the CVC. Since activity began, at ~1·7 Ma (Allan, 1986), volcanism has migrated south through four volcanic centres: Volcán Cántaro, Nevado de Colima, Paleofuego de Colima and Volcán de Colima (Luhr & Carmichael, 1990a; Figs 1 and 2). The evolution of the Nevado and Paleofuego volcanoes has been governed by numerous gravitational collapse events partially destroying what appear to have been large edifices and leaving remnant caldera structures open to the south, SE and SW (Robin *et al.*, 1987; Luhr & Prestegaard, 1988; Luhr & Carmichael, 1990*a*; Stoopes & Sheridan, 1992; Komorowski *et al.*, 1997; Cortés *et al.*, 2009; Norini *et al.*, 2010). The last of these events destroyed the Paleofuego edifice, leaving a semi-circular caldera, which hosts the cone of the currently active Volcán de Colima (Fig. 2).

The CVC lies at the western end of the TMVB ~100 km from the Pacific coast (Fig. 1). The TMVB is an ~1000 km long, ~80–230 km wide, continental volcanic arc comprising over 8000 volcanic centres stretching across central Mexico in an east–west orientation (Gómez-Tuena *et al.*, 2007). The CVC sits within the Colima Rift Zone (CRZ), an ~190 km long, 20–65 km wide zone trending NNE–SSW from Lake Chapala to the Pacific coast (Fig. 1; Allan, 1986). The northern and southern parts of the CRZ are separated by the Tamazula fault zone, which has been interpreted as a basement structure that trends NE–SW, extending for over 160 km and crossing the CRZ at the CVC (Garduño *et al.*, 1998; Cortés *et al.*, 2010; Norini *et al.*, 2010). Garduño *et al.* (1998) proposed that the volcanic activity and recent evolution of the CVC is controlled by the Tamazula fault, specifically the sector-collapse events, which they suggested were triggered by displacement along this fault. The CRZ is thought to have resulted from extension caused by rollback of the Cocos and Rivera plates (Ferrari *et al.*, 2001; Soto *et al.*, 2009; Yang *et al.*, 2009).

The tectonic setting of the western TMVB is complex with convergent and extensional regimes resulting in both subalkaline and alkaline magmatism (Luhr & Carmichael, 1981, 1985; Allan, 1986; Ferrari & Rosas-Elguera, 2000; Ferrari, 2004; Gómez-Tuena *et al.*, 2007; Soto *et al.*, 2009; Yang *et al.*, 2009; Ferrari *et al.*, 2012). To the east and west of the Cántaro and Nevado volcanoes, 11 cinder cones erupted on the rift floor between 1·2 Ma and 62 ka (Fig. 2) (Luhr & Carmichael, 1981; Allan & Carmichael, 1984; Carmichael *et al.*, 2006). The two oldest cones erupted at 1·2 and 0·5 Ma, producing <0·003 km^3 of subalkaline basalt and basaltic andesite (Luhr & Carmichael, 1981; Allan & Carmichael, 1984; Carmichael *et al.*, 2006). Nine of the cinder cones are alkaline, producing ~1·3 km^3 of lava between 450 and 62 ka (Luhr & Carmichael, 1981, 1990*a*; Allan & Carmichael, 1984; Carmichael *et al.*, 2006).

The CVC is dominated by the four subalkaline stratovolcanoes, which have an estimated erupted volume of ~490 km^3, comprising a volcanic apron of andesitic lava flows, debris avalanche deposits, lahars and pyroclastic flow and fall deposits (Cortés *et al.*, 2005, 2010). The alkaline magmas have a much lower total estimated volume of ~1·3 km^3, less than 0·27% of the volume of the CVC subalkaline edifices (Carmichael *et al.*, 2006).

VOLCANIC STRATIGRAPHY

Throughout the 1990s and 2000s numerous field campaigns by the late Jim Luhr and co-workers sampled and described CVC eruption deposits preserved and exposed on the flanks of Nevado de Colima and in quarries and gullies on the rift floor (Fig. 2; Luhr & Carmichael, 1982; Luhr *et al.*, 2010). Through detailed sampling of charcoal discovered within ash horizons and tephra fallout deposits, Luhr *et al.* (2010) defined a detailed eruptive stratigraphy comprising five Plinian fallout deposits erupted between ~6000 a BP and the present day. Further field campaigns carried out as part of this study have built on the work of Luhr *et al.* (2010) on the tephrochronology of the CVC, extending the stratigraphic record back through the Holocene and Late Pleistocene (Crummy, 2013). To date, eruption deposits have been described at 89 localities across an area of ~500 km^2, including exposures in quarries on the rift floor (Fig. 2). Based upon field relationships and geochemical characteristics, these have been stratigraphically subdivided into 15 Plinian tephra fallout units separated by ash-rich pyroclastic flow and surge horizons (units A to α; Fig. 3) following the nomenclature of Luhr *et al.* (2010). The ages of these deposits coincide with the age of Paleofuego prior to the formation of the currently active Volcán de Colima. Based on the shape of the horseshoe scarp in which Volcán de Colima sits, the vent location of Paleofuego can be assumed to be the same as that of the current active vent, but was higher than that of Volcán de Colima with a height of ~4100 m above sea level (Luhr & Carmichael, 1990*a*).

The majority of the tephra fallout deposits exposed on the flanks of Nevado de Colima are medium-K subalkaline basaltic andesite to andesite pumice-fall deposits (Fig. 4), varying in thicknesses from 4 cm to over 1 m at distances of 4–10 km from the vent (Fig. 2, Table 1).

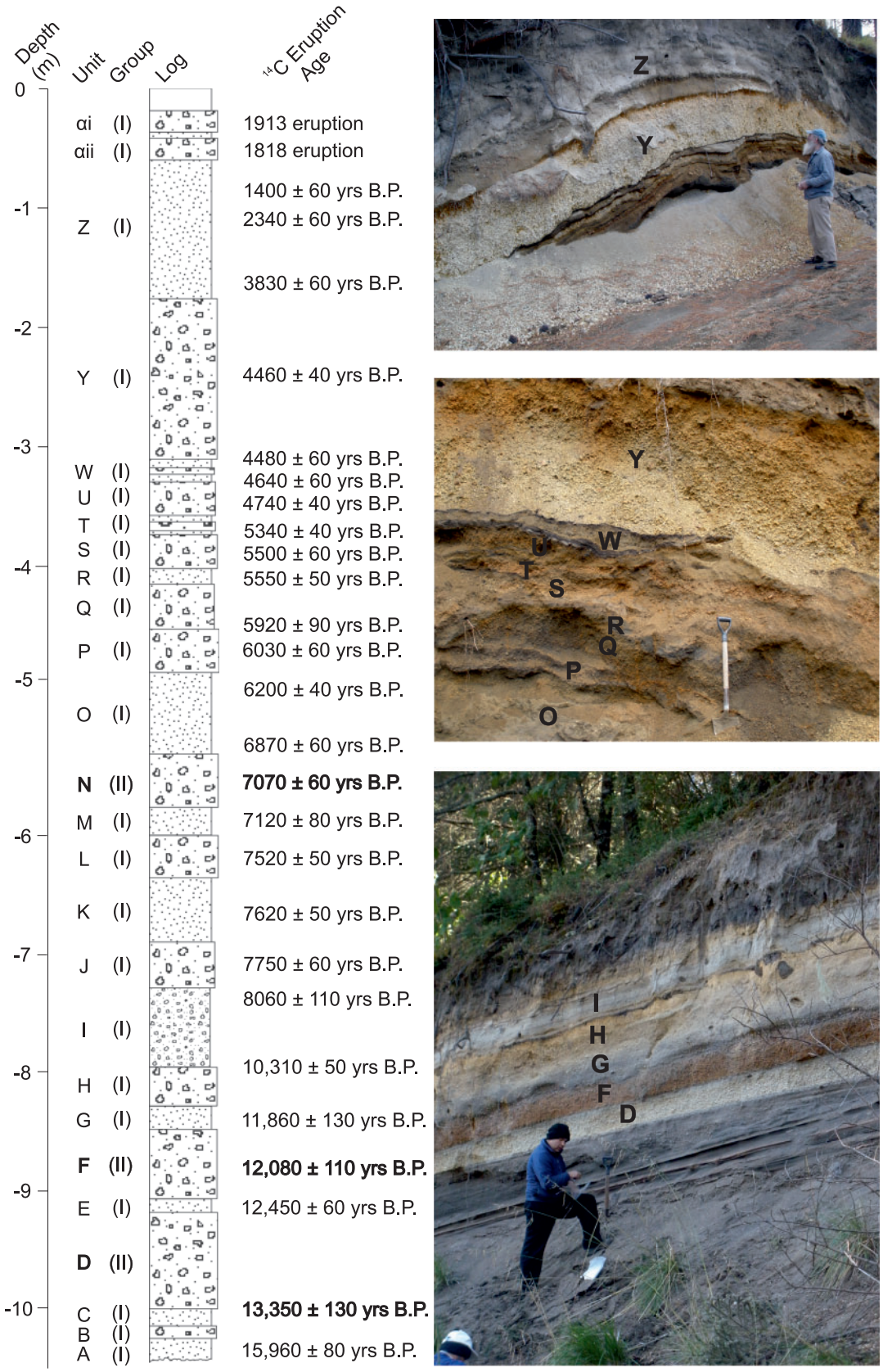

Fig. 3. Composite stratigraphic section from road-cuts on the flanks of Nevado de Colima showing the CVC tephra fallout deposits. The Group II units, N, F and D, are highlighted in bold. Ages are uncalibrated ^{14}C radiocarbon ages from Luhr *et al.* (2010).

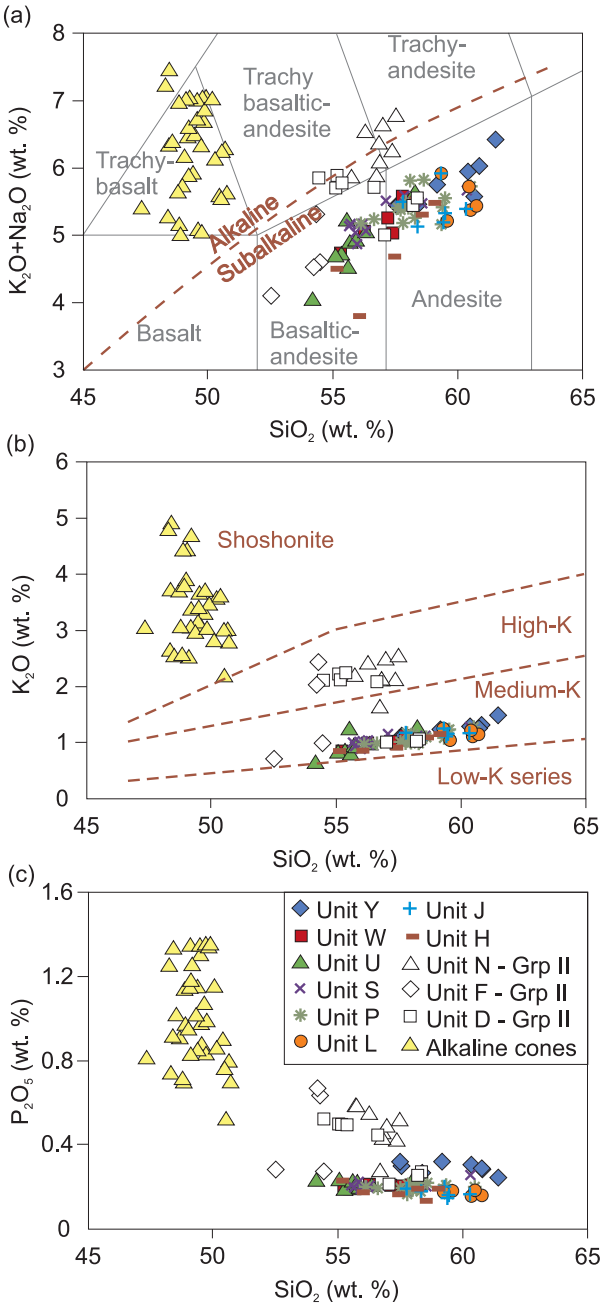

Fig. 4. (a) Total alkalis vs silica (TAS) and (b) K_2O vs SiO_2 classification diagrams after Le Maitre *et al.* (2002). The Group I CVC tephra deposits are medium-K subalkaline basaltic andesites to andesites, whereas the Group II units (white symbols) are typically high-K subalkaline basaltic andesites to trachyandesites. The alkaline cinder cone magmas are shoshonitic trachybasalts. The Group II deposits lie off the main CVC tephra trend on the K_2O (b) and P_2O_5 (c) variation diagrams.

The largest (by volume) deposit is a high-silica andesite in composition (unit Y), which, 10 km from the source vent, has a thickness of 1·4 m (section VF10-04, Fig. 2, Table 2) (Crummy, 2013).

Interbedded within the subalkaline tephra deposits, we discovered three mineralogically and geochemically distinct scoria-fall units that are characterized by the presence of phlogopite, observed both in hand specimen and in thin section, and typically elevated K_2O (up to 2·6 wt %) and P_2O_5 (up to 0·67 wt %) contents relative to the majority of the subalkaline tephra units (Fig. 4). These deposits comprise units N, F and D of the CVC stratigraphy, which erupted at *c.* 7000, 12 000 and 13 000 a BP, respectively (Fig. 3, Table 1). These units are high-K subalkaline, transitional to alkaline, basaltic andesite to trachyandesite in composition (Fig. 4).

Based on the distinctive mineralogical and geochemical characteristics of the fallout deposits, we have divided the CVC tephra into two groups: Group I comprises the bulk of the subalkaline tephra fallout units, whereas Group II comprises the high-K, phlogopite-bearing units N, F and D.

Unit N is a distinctive orange-coloured, inversely graded, basaltic trachyandesite to trachyandesite scoria fall deposit, varying in thickness from 12 to 60 cm at 16 localities between 1 and 10 km from the vent (Fig. 5a, Table 1). Stratigraphically above and below the tephra fallout deposit of unit N are ash layers (Fig. 3). Radiocarbon (^{14}C) ages of charcoal fragments found in these ash horizons constrain the age of unit N to between 6950 ± 50 and 7070 ± 60 a BP (Luhr *et al.*, 2010).

Unit F is a basaltic andesite scoria fall deposit that shows a wide variation in thickness, from 3 to 90 cm, measured at six localities at 2·5–8 km from the vent (Fig. 5b, Table 1). Unit F is a distinctive marker horizon as its scoria clasts contain visible phlogopite phenocrysts. The age of this unit is *c.* 12 000 a BP based on radiocarbon dating of charcoal found within the fall deposit, which yielded ages of 11 840 ± 70 and 12 080 ± 50 a BP (Luhr *et al.*, 2010).

The oldest of the Group II deposits is unit D, which erupted ~13 000 a BP. This unit is a grey basaltic andesite scoria fall deposit with thicknesses ranging from 32 to 180 cm, measured at nine localities 2·5–10 km from the vent (Fig. 5c, Table 1). Charcoal fragments from binding ash layers yielded radiocarbon ages of 12 460 ± 60 and 13 350 ± 130 a BP (Luhr *et al.*, 2010).

Unit N is well correlated across the northern CVC, whereas units F and D are less well correlated with only a limited number of exposures on the lower flanks on the eastern side of Nevado de Colima (Fig. 5).

SAMPLING STRATEGY

Tephra samples were collected from 17 localities across the CVC for petrological and geochemical analysis and granulometry. Owing to a lack of radiocarbon dating and difficulty correlating units, samples ($n = 21$) from five of these localities provide the focus for this study (Table 2).

Table 1: Field characteristics of the CVC eruption deposits

Unit	Eruption age (a BP)	Number of localities	Deposit type	Colour (dry)	Thickness (cm)	Max. pumice (cm)	Max. lithic (cm)	Composition
Y	4460 ± 40	28	Pumice fall	Cream	48–140	17	7	Andesite
W	4480 ± 60 to 4540 ± 60	23	Scoria fall	Dark brown	8–28	6	5	Basaltic andesite
U	4740 ± 40 to 4790 ± 100	30	Scoria fall	Dark orange	15–20	4	2	Basaltic andesite
S	5430 ± 50 to 5500 ± 60	24	Scoria fall	Dark brown–orange	12–46	4·5	2	Basaltic andesite
P	5980 ± 50 to 6150 ± 40	21	Pumice fall	Cream	6–40	9	6	Basaltic andesite
N	**6950 ± 50 to 7070 ± 60**	**16**	**Scoria fall**	**Orange**	**12–60**	**17**	**12**	**Basaltic andesite**
L	7520 ± 50 to 7530 ± 80	16	Scoria fall	Dark brown	4–50	6	3	Andesite
J	7750 ± 60 to 7760 ± 50	8	Pumice fall	Pale orange–cream	7–15	6	3	Basaltic andesite
H	9770 ± 60 to 10 310 ± 50	9	Scoria fall	Dark grey or black	15–42	5	2	Basaltic andesite
F	**11840 ± 70 to 12 080 ± 130**	**6**	**Scoria fall**	**Yellow**	**13–90**	**5**	**8**	**Basaltic andesite**
D	**12460 ± 60 to 13 350 ± 130**	**9**	**Scoria fall**	**Grey**	**32–180**	**6·5**	**5**	**Basaltic andesite**

Group II units (N, F and D) are in bold.

Representative bulk samples (300–1400 g) from each unit were collected; sample sizes were varied to account for the average grain size. Single pumice and scoria clasts from the CVC tephra fallout deposits were selected from the bulk sample for petrological and geochemical analysis. All tephra samples were pre-washed with ultraclean water (UHQ 18 MΩ) and then ultrasonicated, and subsequently dried overnight in an oven at ~90°C. Care was taken to select fresh pumice samples and there was no evidence of post-eruption alteration such as the presence of sericite, chlorite, clay minerals or Fe–Mn oxides and hydroxides.

For each locality, clasts from each unit were selected for polished thin section preparation for optical microscope, scanning electron microscope (SEM) and electron microprobe (EPMA) investigation. Polished thin sections of samples collected by Jim Luhr, on loan from the National Museum of Natural History (Smithsonian Institution) in Washington DC, USA, were also used.

The samples were then crushed and powdered using a mechanical agate pestle and mortar. Pure quartz was crushed between samples and the pestle and mortar were cleaned with acetone to avoid contamination. For whole-rock geochemical analysis, single clasts were used for the very coarse deposits (units Y, S and P), and multiple representative clasts for the finer deposits.

Our data are supplemented by whole-rock geochemical data from Luhr & Carmichael (1981, 1982) and Luhr *et al.* (2010) for the CVC tephra deposits, together with previously unpublished data of Jim Luhr (Tables 3 and 4, and Supplementary Data, Appendix 1; supplementary data are available for downloading at http://www.petrology.oxfordjournals.org). The sample locations are given in Table 2. The whole-rock major and trace element geochemical datasets for the alkaline cinder cones of Luhr & Carmichael (1981), Carmichael *et al.* (2006), Maria & Luhr (2008), Vigouroux *et al.* (2008) and Cai (2009) are also considered here (see Supplementary Data, Appendix 2).

ANALYTICAL TECHNIQUES

Whole-rock major and selected trace element (Sr, Y, Zr, Zn, Co, Cr, Cu, Li, Ni, Sc and V) abundances were determined by inductively coupled plasma atomic emission spectrometry (ICP-AES) at Royal Holloway University of London (RHUL; Table 3). Samples were prepared by $LiBO_2$ flux-fusion for the major elements and Sr, Y, Zr and Zn, and by hydrofluoric–nitric ($HF–HNO_3$) acid digestion for the remaining trace elements (Co, Cr, Cu, Li, Ni, Sc and V).

Whole-rock trace elements (Rb, Nb, Mo, Cs, Hf, Ta, Tl, Th and U) and rare earth elements (REE; La to Lu) were analysed by inductively coupled plasma mass spectrometry (ICP-MS) at RHUL (Table 4) after $HF–HNO_3$ acid digestion, at dilutions of ~1:1000. The ICP-MS data are precise to <0·6%, whereas the ICP-AES data have errors of ~1% (Crummy, 2013).

Strontium and Nd isotope analyses were carried out for nine samples from the high-K mafic eruption deposits (three from unit N, three from unit F and three from unit D) and on 21 samples of the medium-K subalkaline tephra fallout deposits (Table 5). The samples were analysed by thermal ionization mass spectrometry (TIMS) on a Thermo Scientific TRITON-series instrument at the University of Leeds. For $^{87}Sr/^{86}Sr$ analysis, the TIMS was

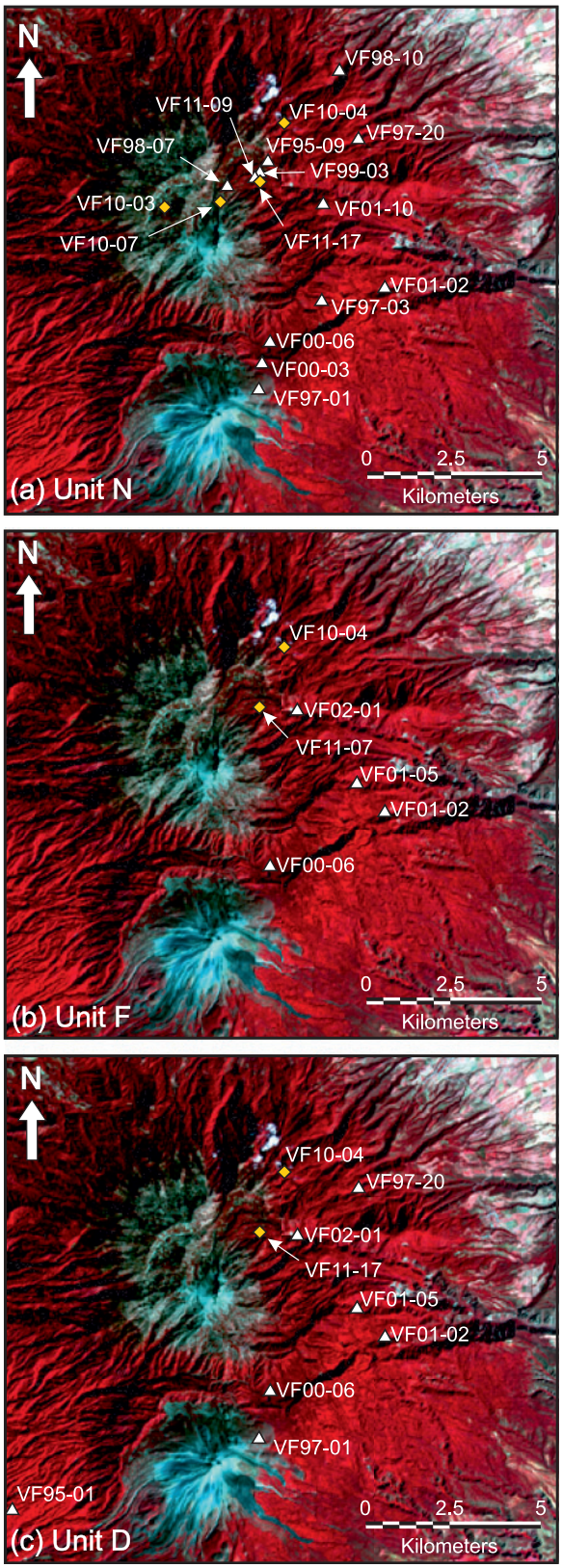

Fig. 5. Location maps for the Group II deposits: (a) unit N; (b) unit F; (c) unit D.

Table 2: Locations of samples used in this study

Locality	Latitude	Longitude
VF94-06	19°33′10″N	103°30′37″W
VF95-01	19°30′00″N	103°42′41″W
VF95-06	19°35′49″N	103°35′14″W
VF95-09	19°35′03″N	103°35′40″W
VF97-01	19°30′57″N	103°38′45″W
VF97-03	19°32′27″N	103°34′53″W
VF97-05	19°38′27″N	103°37′07″W
VF97-06	19°37′15″N	103°36′57″W
VF97-13	19°38′29″N	103°40′34″W
VF97-20	19°35′25″N	103°33′52″W
VF98-02	19°34′55″N	103°36′19″W
VF98-07	19°34′37″N	103°36′28″W
VF98-10	19°36′51″N	103°34′03″W
VF99-03	19°34′39″N	103°35′50″W
VF99-05	19°34′53″N	103°37′12″W
VF00-06	19°31′48″N	103°35′54″W
VF01-01	19°34′49″N	103°35′49″W
VF01-02	19°32′36″N	103°33′32″W
VF01-05	19°33′11″N	103°34′06″W
VF01-10	19°34′12″N	103°34′40″W
VF02-01	19°34′34″N	103°35′08″W
VF10-01	**19°33′38″N**	**103°38′22″W**
VF10-02	**19°33′60″N**	**103°37′52″W**
VF10-03	**19°34′22″N**	**103°37′40″W**
VF10-04	**19°35′47″N**	**103°35′16″W**
VF10-07	**19°34′23″N**	**103°36′36″W**

Samples in bold were collected as part of the present study. The other samples are from field campaigns led by Jim Luhr from 1994 (VF94-XX) to 2002 (VF02-XX).

run in static mode with a ^{88}Sr signal of 3–5 V, with collection of 200 ratios. The internal analytical precision was always better than 5×10^{-6} (2σ). For $^{143}Nd/^{144}Nd$ analysis, the TIMS system was run in static mode at 0·2–0·9 V on ^{144}Nd, until 240 ratios were collected. The internal analytical precision was always better than 9×10^{-6} (2σ). The external precision was monitored via USGS standard BHVO-1 with Sr and Nd isotope ratios averaging 0·703492 ± 66 ($n = 12$) and 0·512970 ± 17 ($n = 8$), respectively. The NBS-987 and La Jolla standards were also run to monitor the external precision on Sr and Nd, respectively. The NBS-987 standard analyses ($n = 58$) averaged 0·71026 ± 4 and La Jolla standard analyses ($n = 23$) averaged 0·51184 ± 3 during the period of this study (2010–2012). All measurements reported here have been normalized to the literature values of NBS-987 (0·710248) and La Jolla (0·51185; Thirlwall, 1991).

Table 3: Whole-rock major and compatible trace element data for the Group I and Group II tephra samples

Sample:	VF10-01U	VF10-02U	VF10-03U	VF10-07U	VF01-01T	VF10-07S	VF10-07Q	VF10-01S	VF10-02S	VF10-03S	VF10-07M1	VF10-02P	VF10-01P
Unit:	U	U	U	U	U	S	S	S	S	S	S	P	P
Group:	I	I	I	I	I	I	I	I	I	I	I	I	I
Age (a BP):	4700	4700	4700	4700	4700	5500	5500	5500	5500	5500	5500	6000	6000
Reference:	1	1	1	1	2	1	1	1	1	1	1	1	1
SiO_2	56·34	55·05	55·80	55·65	54·17	55·72	57·06	56·14	58·56	60·33	58·60	57·98	56·11
TiO_2	0·79	0·74	0·68	0·71	0·81	0·81	0·76	0·71	0·64	0·54	0·59	0·72	0·77
Al_2O_3	18·63	18·13	17·61	18·91	19·36	18·18	17·11	17·57	17·21	17·33	19·80	17·87	18·51
FeO_T	6·95	7·35	7·29	6·87	7·27	7·28	6·95	6·92	6·36	5·94	5·63	6·56	6·98
MnO	0·11	0·12	0·11	0·11	0·12	0·11	0·12	0·11	0·10	0·10	0·09	0·11	0·11
MgO	4·66	6·06	6·13	5·17	6·09	5·05	5·45	5·69	4·95	4·13	2·60	4·61	4·95
CaO	7·23	7·62	7·17	7·39	7·38	7·46	6·81	7·47	6·50	5·74	6·64	6·56	7·19
Na_2O	4·10	3·85	4·05	4·02	3·41	4·15	4·39	4·16	4·35	4·37	4·73	4·27	4·20
K_2O	1·00	0·84	0·95	0·94	0·67	1·02	1·15	1·01	1·12	1·28	1·10	1·12	0·98
P_2O_5	0·21	0·24	0·22	0·22	0·24	0·21	0·21	0·22	0·20	0·25	0·22	0·20	0·20
Total	100	100	100	100	100	100	100	100	100	100	100	100	100
V	155	148	149	153	127	142	148	156	129	119	113	145	156
Cr	102	198	177	157	199	112	122	172	143	126	22	107	116
Co	21	22	23	21	27	21	19	21	17	16	13	19	21
Ni	44	69	75	58	79	54	42	68	44	49	13	38	49
Cu	35	39	42	41	43	36	27	42	22	20	18	31	32
Zn	69	61	69	59	70	73	75	63	71	85	66	70	66
Rb	–	–	–	–	7	–	–	–	–	–	–	–	–
Sr	658	618	575	624	627	666	593	615	604	564	679	558	627
Y	18	17	18	18	18	19	18	17	17	16	17	18	17
Zr	109	109	101	110	158	109	115	104	109	111	112	117	105
Nb	–	–	–	–	9	–	–	–	–	–	–	–	–
Ba	–	–	–	–	280	–	–	–	–	–	–	–	–

Sample:	VF10-04M	VF10-04N	VF10-07M_3	VF01-10D	VF95-09G	VF98-07D	VF98-10O	VF99-03R	VF10-07D	VF97-03BJ	VF10-03N	VF10-07B	VF10-03M_2
Unit:	Pi	Ps	P	N	N	N	N	N	N	N	N	L	L
Group:	I	I	I	II	II	II	II	II	II	II	II	I	I
Age (a BP):	6000	6000	6000	7000	7000	7000	7000	7000	7000	7000	7000	7500	7500
Reference:	1	1	1	2	2	2	2	2	1	2	1	1	1
SiO_2	59·47	56·63	58·08	57·37	56·82	56·96	57·48	56·83	56·29	56·71	55·75	60·52	60·40
TiO_2	0·48	0·71	0·70	0·81	0·85	0·86	0·83	0·85	0·80	0·79	0·91	0·56	0·55
Al_2O_3	18·98	19·38	19·02	17·52	17·80	18·59	18·09	18·38	18·44	16·37	19·86	17·50	17·55
FeO_T	5·50	7·07	6·29	6·06	6·04	6·14	5·96	6·21	6·97	6·03	7·31	5·54	5·41
MnO	0·08	0·10	0·10	0·11	0·11	0·11	0·11	0·11	0·12	0·11	0·11	0·10	0·09
MgO	3·88	4·18	3·29	4·46	4·39	3·46	3·51	4·24	3·90	6·27	3·53	4·27	4·09
CaO	5·89	6·50	6·51	6·69	6·82	6·33	6·31	6·49	6·38	7·26	6·05	5·98	6·03
Na_2O	4·32	4·24	4·67	4·11	4·22	4·16	4·21	3·99	4·12	4·25	3·67	4·23	4·49
K_2O	1·22	0·99	1·14	2·15	2·15	2·50	2·58	2·11	2·43	1·64	2·20	1·11	1·24

(continued)

Table 3: Continued

Sample:	VF10-04M	VF10-04N	VF10-07M$_3$	VF01-10D	VF95-09G	VF98-07D	VF98-10O	VF99-03R	VF10-07D	VF97-03BJ	VF10-03N	VF10-07B	VF10-03M$_2$
Unit:	Pi	Ps	P	N	N	N	N	N	N	N	N	L	L
Group:	I	I	I	II	II	II	II	II	II	II	II	I	I
Age (a BP):	6000	6000	6000	7000	7000	7000	7000	7000	7000	7000	7000	7500	7500
Reference:	1	1	1	2	2	2	2	2	1	2	1	1	1
P_2O_5	0·16	0·19	0·20	0·43	0·46	0·49	0·52	0·44	0·55	0·28	0·59	0·18	0·15
Total	100	100	100	100	100	100	100	100	100	100	100	100	100
V	102	137	133	122	163	165	162	149	150	157	141	108	111
Cr	105	71	39	131	102	68	67	111	71	279	80	157	125
Co	14	17	15	21	20	18	18	20	17	26	17	15	16
Ni	37	33	21	54	44	35	36	48	36	100	34	49	49
Cu	25	29	27	42	45	47	44	44	49	36	52	22	22
Zn	53	68	70	85	75	80	81	76	78	67	102	60	70
Rb	–	–	–	26	30	28	30	24	–	21	–	–	–
Sr	539	615	654	1247	1318	1466	1422	1282	1423	962	1308	636	628
Y	14	16	18	21	20	20	19	20	22	18	22	14	13
Zr	122	111	113	281	212	248	241	227	222	177	234	108	101
Nb	–	–	–	2	6	4	3	8	–	5	–	–	–
Ba	–	–	–	916	989	1036	1103	977	–	677	–	–	–

Sample:	VF10-04F	VF00-06Pi	VF00-06Ps	VF01-02Pi	VF95-01B	VF95-01C	VF01-02Ni	VF00-06Os	VF01-05N	VF97-20D	VF00-06Oi	VF01-02Ns
Unit:	F	F	F	F	D	D	D	D	D	D	D	D
Group:	II	II	II	II	II	II	II	II	II	II	II	II
Age (a BP):	12000	12000	12000	12000	13000	13000	13000	13000	13000	13000	13000	13000
Reference:	1	2	2	2	2	2	2	2	2	2	2	2
SiO_2	52·52	54·30	54·47	54·22	58·32	58·20	56·61	54·46	55·09	57·06	55·15	55·35
TiO_2	0·88	1·02	0·87	1·04	0·81	0·81	0·89	0·92	0·91	0·75	0·92	0·90
Al_2O_3	17·84	14·96	17·78	15·63	18·86	19·16	16·62	16·42	16·15	18·54	16·37	16·31
FeO_T	8·59	7·17	7·17	7·34	6·38	6·35	6·73	7·07	6·96	6·18	6·96	6·94
MnO	0·12	0·11	0·13	0·13	0·13	0·12	0·12	0·13	0·12	0·11	0·13	0·12
MgO	7·63	7·59	6·57	7·89	2·93	2·89	5·21	6·09	6·17	4·93	5·91	5·92
CaO	8·05	8·39	7·73	8·04	6·49	6·52	7·32	8·12	8·03	6·96	7·78	7·84
Na_2O	3·39	2·88	3·62	2·53	4·44	4·41	3·63	3·73	3·49	4·05	3·76	3·54
K_2O	0·70	2·43	1·00	2·01	1·08	1·02	2·09	2·11	2·23	0·98	2·12	2·25
P_2O_5	0·28	0·63	0·28	0·67	0·26	0·24	0·45	0·52	0·50	0·21	0·49	0·49
Total	100	100	100	100	100	100	100	100	100	100	100	100
V	177	149	142	146	137	141	132	144	142	151	138	140
Cr	205	299	209	292	12	<3	101	146	159	92	143	148
Co	27	29	29	28	20	21	24	25	26	21	25	25
Ni	69	98	98	109	17	17	29	41	42	51	41	40
Cu	42	85	54	89	39	36	48	66	54	36	61	54
Zn	73	82	80	111	76	71	84	85	84	69	86	84

(continued)

Table 3: Continued

Sample:	VF10-04F	VF00-06Pi	VF00-06Ps	VF01-02Pi	VF95-01B	VF95-01C	VF01-02Ni	VF00-06Os	VF01-05N	VF97-20D	VF00-06Oi	VF01-02Ns
Unit:	F	F	F	F	D	D	D	D	D	D	D	D
Group:	II	II	II	II	II	II	II	II	II	II	II	II
Age (a BP):	12000	12000	12000	12000	13000	13000	13000	13000	13000	13000	13000	13000
Reference:	1	2	2	2	2	2	2	2	2	2	2	2
Rb	–	19	8	16	15	12	21	23	24	12	22	21
Sr	578	2540	1033	2296	680	624	1288	1398	1395	619	1346	1381
Y	20	19	17	19	20	21	22	22	21	17	22	21
Zr	125	304	153	384	158	150	276	285	288	137	280	278
Nb	–	9	4	6	3	7	5	5	5	<2	6	5
Ba	–	1844	539	1769	430	395	812	842	808	461	812	820

References: 1, this study; whole-rock major and selected trace elements (Sr, Y, Zr, Zn, Co, Cr, Cu, Li, Ni, Sc and V) analysed by ICP-AES at Royal Holloway University of London; 2, unpublished dataset of Jim Luhr; whole-rock major and selected trace elements (Ba, Sr, Y, Zr, Zn, Co, Cr, Cu, Li, Ni, Sc and V) analysed by XRF.

SEM and EPMA investigations were carried out using FEI Quanta 650 FEG-ESEM and JEOL 8230 instruments at the University of Leeds. The analytical conditions for the electron microprobe analysis of mafic minerals were 15 kV accelerating potential and 15 nA beam current, and 15 kV accelerating potential and 10 nA beam current for plagioclase and glass analyses. The analytical conditions were maintained similar to those used in the previous studies of Colima eruption deposits by Savov *et al.* (2008) and Luhr *et al.* (2010).

WHOLE-ROCK GEOCHEMISTRY AND CLASSIFICATION

Major elements

The majority of the tephra fallout deposits are medium-K subalkaline basaltic andesite (54·2 wt % SiO_2) to andesite (61·5 wt % SiO_2) in composition (Fig. 4a; Table 3), and follow a differentiation trend of increasing K_2O and Na_2O and decreasing MgO, CaO, FeO_T, TiO_2 and P_2O_5 with increasing SiO_2 (Fig. 6). All whole-rock major element data have been normalized to 100% on an anhydrous basis. Samples with loss on ignition (LOI) > 4 wt % were omitted owing to probable alteration during post-eruptive weathering.

Scoria samples from the Group II units N, F and D are high-K subalkaline, transitional to alkaline, basalt to trachyandesite in composition (52·5–58·3 wt % SiO_2; Fig. 4; Table 3). Unit F is the most mafic of the Group II units, with SiO_2 varying from 52·5 to 54·5 wt %. The SiO_2 contents in units N and D range from 55·7 to 57·5 and 54·5 to 58·3 wt %, respectively (Fig. 4a; Table 3). Overall, these three eruption deposits follow a similar differentiation trend to the majority of the subalkaline Group I units, of increasing K_2O and Na_2O and decreasing MgO, CaO, FeOt, TiO_2 and P_2O_5 with increasing SiO_2 (Fig. 6). Many of the samples, however, display characteristically elevated K_2O (up to 2·6 wt %) and P_2O_5 (up to 0·67 wt %) relative to the medium-K subalkaline CVC series (0·67–1·48 wt % K_2O; 0·13–0·33 wt % P_2O_5; Figs 4b, c and 6). Two samples from unit F (VF10-04F and VF00-06Ps) and three samples from unit D (VF95-01B, VF95-01C and VF97-20D) are geochemically more similar to the Group I medium-K subalkaline deposits: these samples do not show the strong K_2O and P_2O_5 enrichments characteristic of the Group II units to which these samples belong (Figs 4 and 6).

The alkaline magmas that formed monogenetic cinder cones on the Colima Rift floor were first described by Luhr & Carmichael (1981) as primitive basanites to minette lamprophyres. The deposits are mafic, with SiO_2 concentrations of 47·3–50·7 wt %, MgO concentrations of 6·2–15·4 wt % and 2·2–4·9 wt % K_2O (Luhr & Carmichael, 1981; Carmichael *et al.*, 2006; Maria & Luhr, 2008; Vigouroux *et al.*, 2008; Cai, 2009). According to the total alkalis–silica and K_2O classification diagrams of Le Maitre *et al.* (2002), they are shoshonitic, alkaline trachybasalts in composition (Fig. 4). Samples from the alkaline cinder cones have high TiO_2, FeO_T, MgO and CaO, and low Al_2O_3 and Na_2O relative to samples from the CVC subalkaline tephra fallout deposits (Fig. 6).

Trace elements

The compatible trace elements in the CVC fallout deposits follow an overall differentiation trend of decreasing Cr and Ni with increasing SiO_2 (Fig. 6). Compatible trace

Table 4: Whole-rock trace element ICP-MS data for the Group I and Group II tephra samples

Sample:	VF10-01U	VF10-02U	VF10-03U	VF10-07U	VF10-01S	VF10-02S	VF10-03S	VF10-02P	VF10-01P	VF10-04M	VF10-04N
Unit:	U	U	U	U	S	S	S	P	P	P	P
Group:	I	I	I	I	I	I	I	I	I	I	I
Age (a BP):	4700	4700	4700	4700	5500	5500	5500	6000	6000	6000	6000
Reference:	1	1	1	1	1	1	1	1	1	1	1
Sc	–	–	–	–	–	–	–	–	–	–	–
Rb	12·7	9·1	10·1	10·3	11·4	12·8	15·5	14·3	11·3	15·5	11·4
Sr	–	–	–	–	–	–	–	–	–	–	–
Y	–	–	–	–	–	–	–	–	–	–	–
Zr	–	–	–	–	–	–	–	–	–	–	–
Nb	3·91	4·66	4·40	5·21	4·40	–	3·58	3·19	3·42	2·97	3·27
Cs	0·48	0·44	0·38	0·35	0·43	0·68	0·61	0·58	0·44	0·54	0·43
Ba	–	–	–	–	–	–	–	–	–	–	–
La	11·82	10·74	10·58	10·76	10·41	10·48	11·61	10·78	11·18	10·95	8·93
Ce	25·16	22·36	22·82	23·11	22·57	21·37	23·96	23·01	23·34	21·97	19·71
Pr	3·56	3·10	3·15	3·25	3·02	3·08	3·17	3·17	3·26	2·81	2·67
Nd	15·99	14·20	14·07	14·47	13·64	13·61	13·64	14·32	14·75	11·96	11·93
Sm	3·66	3·42	3·42	3·37	3·31	3·26	3·10	3·40	3·50	2·74	2·92
Eu	1·14	1·04	1·00	1·00	0·96	0·96	0·88	1·75	1·03	0·79	0·87
Gd	3·28	2·92	2·91	2·98	2·89	2·83	2·67	2·93	3·01	2·26	2·64
Tb	0·54	0·51	0·53	0·50	0·49	0·48	0·45	0·51	0·50	0·40	0·44
Dy	2·78	2·73	2·66	2·59	2·55	2·48	2·38	2·73	2·69	2·10	2·40
Ho	0·56	0·56	0·55	0·60	0·54	0·53	0·49	0·57	0·54	0·42	0·51
Er	1·52	1·52	1·49	1·49	1·45	1·44	1·34	1·51	1·43	1·18	1·35
Tm	0·23	0·24	0·23	0·24	0·22	0·21	0·21	0·2	0·23	0·18	0·21
Yb	1·54	1·59	1·62	1·59	1·61	1·53	1·47	1·70	1·49	1·29	1·53
Lu	0·22	0·22	0·24	0·22	0·22	0·22	0·21	0·24	0·22	0·21	0·20
Hf	2·72	3·00	2·62	1·98	2·56	2·73	3·13	2·97	2·57	3·08	2·71
Ta	0·24	0·30	0·28	0·29	0·29	–	0·28	0·23	0·30	0·23	0·23
Pb	–	–	–	–	–	–	–	–	–	–	–
Th	1·72	1·38	1·30	1·36	1·42	1·67	1·78	1·66	1·33	1·86	1·22
U	0·39	0·38	0·41	0·31	0·53	0·41	0·54	0·50	0·67	0·54	0·53

Sample:	VF01-10D	VF95-09G	VF10-07D	VF97-03BJ	VF10-03N	VF10-07B	VF10-03M2	VF10-04F	VF00-06Pi	VF00-06Ps	VF01-02Pi
Unit:	N	N	N	N	N	L	L	F	F	F	F
Group:	II	II	II	II	II	I	I	II	II	II	II
Age (a BP):	7000	7000	7000	7000	7000	7500	7500	12000	12000	12000	12000
Reference:	2	2	1	2	1	1	1	1	2	2	2
Sc	14·7	15·3	–	21·0	–	–	–	–	26·3	25·4	27·0
Rb	26·4	27·0	26·7	20·6	26·0	13·9	13·9	6·9	20·6	9·0	17·1
Sr	1257	1333	–	933	–	–	–	–	2548	990	2171
Y	20·94	20·29	–	18·68	–	–	–	–	18·25	17·62	20·13
Zr	194	–	–	–	–	–	–	–	207	112	211
Nb	4·26	4·46	4·39	3·62	4·55	2·74	2·88	3·63	4·94	3·23	4·98

(continued)

Table 4: Continued

Sample:	VF01-10D	VF95-09G	VF10-07D	VF97-03BJ	VF10-03N	VF10-07B	VF10-03M2	VF10-04F	VF00-06Pi	VF00-06Ps	VF01-02Pi
Unit:	N	N	N	N	N	L	L	F	F	F	F
Group:	II	II	II	II	II	I	I	II	II	II	II
Age (a BP):	7000	7000	7000	7000	7000	7500	7500	12000	12000	12000	12000
Reference:	2	2	1	2	1	1	1	1	2	2	2
Cs	0·60	0·61	0·57	0·51	1·17	0·51	0·60	0·29	0·34	0·22	0·39
Ba	969	969	–	685	–	–	–	–	1826	571	1667
La	33·12	33·35	36·70	21·06	35·38	8·82	8·46	19·35	54·86	18·51	61·01
Ce	68·55	70·25	81·25	45·25	73·13	18·29	18·12	38·14	110·58	36·96	116·48
Pr	8·80	9·01	10·68	5·82	10·64	2·51	2·41	5·97	13·84	5·03	15·34
Nd	36·11	37·30	45·19	25·17	44·84	11·09	10·64	25·48	57·11	21·58	62·84
Sm	7·19	7·07	8·18	5·43	8·03	2·69	2·56	5·36	10·19	4·63	10·98
Eu	1·96	1·98	2·07	1·64	2·08	0·81	0·85	1·41	2·64	1·44	2·86
Gd	5·37	5·17	5·69	4·39	5·71	2·38	2·24	4·20	6·63	3·89	7·16
Tb	0·72	0·74	0·82	0·63	0·80	0·41	0·40	0·68	0·77	0·59	0·82
Dy	3·96	3·91	3·39	3·44	3·54	2·12	1·97	3·24	3·81	3·39	4·17
Ho	0·74	0·73	0·65	0·66	0·68	0·43	0·40	0·64	0·68	0·66	0·73
Er	1·97	1·90	1·76	1·76	1·84	1·15	1·14	1·77	1·66	1·79	1·84
Tm	0·28	0·28	0·26	0·25	0·27	0·18	0·17	0·26	0·23	0·25	0·25
Yb	1·77	1·68	1·88	1·58	1·86	1·30	1·13	1·79	1·35	1·59	1·47
Lu	0·28	0·26	0·28	0·25	0·26	0·18	0·17	0·25	0·21	0·25	0·23
Hf	5·34	5·23	5·60	3·89	5·58	2·70	2·57	3·18	5·98	3·24	6·30
Ta	0·26	0·26	0·29	0·24	0·33	0·22	0·20	0·22	0·25	0·19	0·25
Pb	9·51	9·77	–	7·17	–	–	–	–	21·17	7·71	21·76
Th	3·61	3·96	4·50	2·53	4·24	1·15	1·0	1·66	4·98	1·55	5·21
U	1·11	1·26	1·28	0·88	1·55	0·39	0·28	0·55	1·41	0·58	1·44

Sample:	VF01-02Ps	VF01-05PA	VF01-02Ni	VF00-06Os	VF01-05N	VF00-06Oi	VF01-02Ns
Unit:	F	F	D	D	D	D	D
Group:	II	II	II	II	II	II	II
Age (a BP):	12000	12000	13000	13000	13000	13000	13000
Reference:	2	2	2	2	2	2	2
Sc	30·8	29·8	22·0	25·1	24·5	24·2	23·9
Rb	6·1	8·9	22·5	22·2	22·8	22·2	23·2
Sr	2544	1798	1229	1478	1346	1360	1320
Y	20·63	22·30	21·24	21·70	21·29	21·01	20·98
Zr	244	241	173	185	182	179	179
Nb	5·94	5·64	4·09	3·96	3·89	3·93	3·88
Cs	0·20	0·22	0·45	0·40	0·42	0·40	0·43
Ba	1606	1270	803	865	803	800	810
La	61·44	67·64	35·37	37·29	37·42	37·02	36·53
Ce	134·72	107·04	73·85	81·13	79·48	78·21	77·84
Pr	16·14	17·70	9·72	10·70	10·47	10·32	10·33
Nd	64·96	70·71	42·31	46·78	45·43	44·63	44·06

(continued)

Table 4: Continued

Sample:	VF01-02Ps	VF01-05PA	VF01-02Ni	VF00-06Os	VF01-05N	VF00-06Oi	VF01-02Ns
Unit:	F	F	D	D	D	D	D
Group:	II	II	II	II	II	II	II
Age (a BP):	12000	12000	13000	13000	13000	13000	13000
Reference:	2	2	2	2	2	2	2
Sm	11·17	12·27	8·65	9·57	9·34	9·04	8·94
Eu	2·91	3·12	2·42	2·54	2·54	2·47	2·39
Gd	7·51	7·59	6·38	6·95	6·85	6·47	6·45
Tb	0·91	0·93	0·81	0·86	0·86	0·83	0·82
Dy	4·66	4·62	4·10	4·44	4·27	4·24	4·12
Ho	0·82	0·80	0·77	0·80	0·77	0·76	0·77
Er	2·05	2·00	1·99	2·07	1·93	1·97	1·94
Tm	0·28	0·28	0·27	0·28	0·28	0·26	0·27
Yb	1·70	1·68	1·67	1·69	1·65	1·63	1·64
Lu	0·26	0·25	0·26	0·26	0·26	0·25	0·25
Hf	7·15	7·10	4·73	5·09	5·02	5·04	4·93
Ta	0·31	0·29	0·24	0·23	0·23	0·23	0·22
Pb	23·15	23·64	9·76	10·02	10·15	9·73	9·52
Th	5·50	5·70	3·79	4·24	4·31	4·11	4·09
U	1·69	1·46	1·22	1·27	1·33	1·28	1·27

References: 1, this study; 2, unpublished dataset of Jim Luhr.

elements abundances in units N, F and D are consistent with this trend, whereas the alkaline cinder cone deposits have higher and more variable compatible trace element concentrations relative to the CVC subalkaline tephra (Fig. 6).

Normal mid-ocean ridge basalt (N-MORB)-normalized incompatible trace element abundance patterns reveal enrichments in large ion lithophile elements (LILE; Rb, Ba, K, Sr Th) relative to high field strength elements (HFSE: Nb, Ta, Ti, Hf, Zr), consistent with those of typical subduction-related magmas characterized by addition of slab-derived fluids to their mantle source (Fig. 7; Saunders *et al.*, 1991). However, in comparison with the majority of the CVC medium-K subalkaline Group I deposits, units N, F and D have elevated incompatible trace element and REE abundances (Fig. 7). Typically, unit F displays the strongest LILE and light REE (LREE) enrichments (Fig. 7). However, two samples from unit F (VF10-04F and VF00-06Ps) are less enriched than the other unit F samples and again show more affinity to the Group I samples, as observed in the major element plots (Fig. 7c). One sample from unit N (VF97-03BJ) also reveals a trend towards the Group I compositions (Fig. 7b). Unfortunately, there are no ICP-MS trace element data for the unit D samples that are geochemically similar to the Group I units in terms of major element data.

The same variation in the units can be seen more clearly on incompatible trace element variation diagrams (Fig. 8). The majority of the Group II samples are strongly enriched in the fluid-mobile elements K, Sr and Ba. Unit F shows the strongest enrichment in Sr and Ba, whereas units N and D are less enriched than unit F, but more enriched than the Group I medium-K subalkaline units. Two unit F, three unit D and one unit N sample are compositionally more similar to the Group I samples with less enriched K, Sr and Ba (Fig. 8). These are the same samples that have the major and trace element variations described above.

The high-K, alkaline cinder cone magmas all display characteristic subduction-related trace element abundance patterns (Figs 7 and 8) with highly enriched LILE (Ba, K, Sr) relative to HFSE (Ta, Nb, Hf, Ti) abundances (Luhr & Carmichael, 1981; Carmichael *et al.*, 2006; Maria & Luhr, 2008; Vigouroux *et al.*, 2008; Cai, 2009). The incompatible element concentrations within the alkaline scoria cone samples are strongly enriched relative to the Group I medium-K subalkaline samples, but overlap the Group II high-K subalkaline transitional to alkaline deposits (Fig. 7).

Whole-rock isotope geochemistry

Strontium and Nd isotopes are widely used to fingerprint magma source(s) and identify open- and closed-system

Table 5: Whole-rock Sr and Nd isotopic ratios for the CVC tephra fallout deposits analysed as part of this study

Sample	Unit	$^{87}Sr/^{86}Sr$	2σ error ($\times10^{-6}$)	$^{143}Nd/^{144}Nd$	2σ error ($\times10^{-6}$)
VF95-09X	Y	0·703627	±4	0·512940	±11
VF97-06D	Y	0·703633	±6	0·512912	±4
VF97-13B	Y	0·703623	±6	0·512916	±6
VF98-02W	W	0·703582	±4	0·512916	±6
VF95-06W	W	0·703574	±6	0·512941	±8
VF10-01U	U	0·703586	±4	0·512924	±6
VF10-02U	U	0·703593	±4	0·512932	±6
VF10-04U	U	0·703635	±5	0·512921	±7
VF10-07U	U	0·703594	±4	0·512934	±4
VF95-06P	S	0·703555	±4	0·512953	±3
VF95-09T	S	0·703592	±4	0·512932	±6
VF10-03Q	P	0·703577	±13	0·512948	±5
VF10-07M3	P	0·703604	±4	0·512927	±5
VF10-01P	P	0·703564	±4	0·512948	±7
VF10-03Pi	P	0·703557	±10	0·512902	±7
VF10-07D	**N**	**0·703723**	**±3**	**0·512908**	**±6**
VF95-09G	**N**	**0·703711**	**±4**	**0·512916**	**±4**
VF10-03N	**N**	**0·703711**	**±4**	**0·512922**	**±4**
VF95-09E	L	0·703597	±3	0·512909	±5
VF10-03M2	L	0·703604	±4	0·512932	±8
VF10-03L	J	0·703610	±4	0·512937	±6
VF00-06R	H	0·703384	±3	0·512952	±5
VF94-06E	H	0·703705	±5	0·512913	±5
VF97-01Di	H	0·703689	±5	0·512913	±5
VF01-02Ps	**F**	**0·704084**	**±4**	**0·512791**	**±4**
VF01-05PA	**F**	**0·704044**	**±4**	**0·512787**	**±5**
VF10-04F	**F**	**0·703681**	**±4**	**0·512913**	**±5**
VF95-01B	**D**	**0·703645**	**±5**	**0·512936**	**±5**
VF01-02Ni	**D**	**0·703696**	**±4**	**0·512920**	**±10**
VF01-05N	**D**	**0·703695**	**±4**	**0·512908**	**±5**
1004-500	–	*0·70385*	*±3*	*0·51286*	*±1*
SAY-101B	–	*0·70383*	*±3*	*0·51287*	*±1*
SAY-7E	–	*0·70417*	*±3*	*0·51277*	*±1*
SAY-8H	–	*0·70381*	*±3*	*0·51283*	*±1*

The Group II deposits are in bold, and the alkaline cinder cones from Cai (2009) are in italics.

processes occurring in the magma storage region, such as magma mixing, crustal assimilation and fractional crystallization (AFC; e.g. Tatsumi *et al.*, 1992; Straub *et al.*, 2010; Verma & Luhr, 2010; Schmidt & Grunder, 2011). The majority of the CVC medium-K subalkaline tephra have narrow ranges of whole-rock $^{87}Sr/^{86}Sr$ and $^{143}Nd/^{144}Nd$, varying from 0·70338 to 0·70371 and 0·51290 to 0·51295, respectively (Table 5, Fig. 9a), consistent with previously published whole-rock Sr–Nd isotope data for CVC lavas (Valdez-Moreno *et al.*, 2006; Verma & Luhr, 2010). The Group I magmas show very little variation in $^{87}Sr/^{86}Sr$ and $^{143}Nd/^{144}Nd$ with increasing SiO_2 (Fig. 9b and c).

The high-K mafic Group II units display slightly higher $^{87}Sr/^{86}Sr$ and lower $^{143}Nd/^{144}Nd$ than the majority of the CVC tephras (Fig. 9). Units N and D of the high-K mafic tephras display a narrow range in $^{87}Sr/^{86}Sr$ and $^{143}Nd/^{144}Nd$, varying from 0·70365 to 0·70372 and 0·51291 to 0·51294, respectively (Table 5; Fig. 9). Unit F displays a much wider range in $^{87}Sr/^{86}Sr$ (0·70368–0·70408) and $^{143}Nd/^{144}Nd$ (0·51279–0·51291). However, there is a clear distinction within unit F samples; two of the unit F samples, VF01-02Ps and VF01-05PA, have more radiogenic $^{87}Sr/^{86}Sr$ ratios of 0·70404 and 0·70408, and less radiogenic $^{143}Nd/^{144}Nd$ ratios of 0·512787 and 0·512791, respectively. These two samples have LOI values of 5·14 and 7·47, respectively, indicating possible post-eruption alteration. $^{87}Sr/^{86}Sr$ could have been modified by interaction with groundwater that had equilibrated with local crustal rocks; however, Nd is immobile during weathering, therefore, the less radiogenic $^{143}Nd/^{144}Nd$ ratios of these two samples can be considered magmatic. As such, we believe these values are primary and have not resulted from secondary alteration processes. The unit F sample that displays less radiogenic $^{87}Sr/^{86}Sr$ and more radiogenic $^{143}Nd/^{144}Nd$, similar to the Group I tephra compositions, is VF10-04F, which is also compositionally similar to the Group I samples in terms of whole-rock major and trace element geochemistry, as described above.

Whole-rock $^{87}Sr/^{86}Sr$ and $^{143}Nd/^{144}Nd$ data are available for samples from only four of the local alkaline cinder cones (Cai, 2009). These samples have more radiogenic $^{87}Sr/^{86}Sr$ (0·70381–0·70417) and less radiogenic $^{143}Nd/^{144}Nd$ (0·51277–0·51287) relative to the medium-K Group I eruption deposits and the majority of the high-K Group II units (Fig. 9, Table 5).

PETROGRAPHY AND MINERAL CHEMISTRY

Mineralogy

The Group I eruption deposits are typical arc basaltic andesites to andesites with the mineral assemblage plagioclase + clinopyroxene + orthopyroxene + amphibole + Fe–Ti oxides ± olivine in varying amounts (Table 6). Scoria and pumice are typically highly vesiculated with phenocryst and microphenocryst (<0·3 mm after Wilcox, 1954) phases making up 10–25 vol. %. The groundmass comprises highly vesiculated glass with abundant microlites of the same mineral phases, with the exception of amphibole, which is absent from the groundmass. Gabbroic

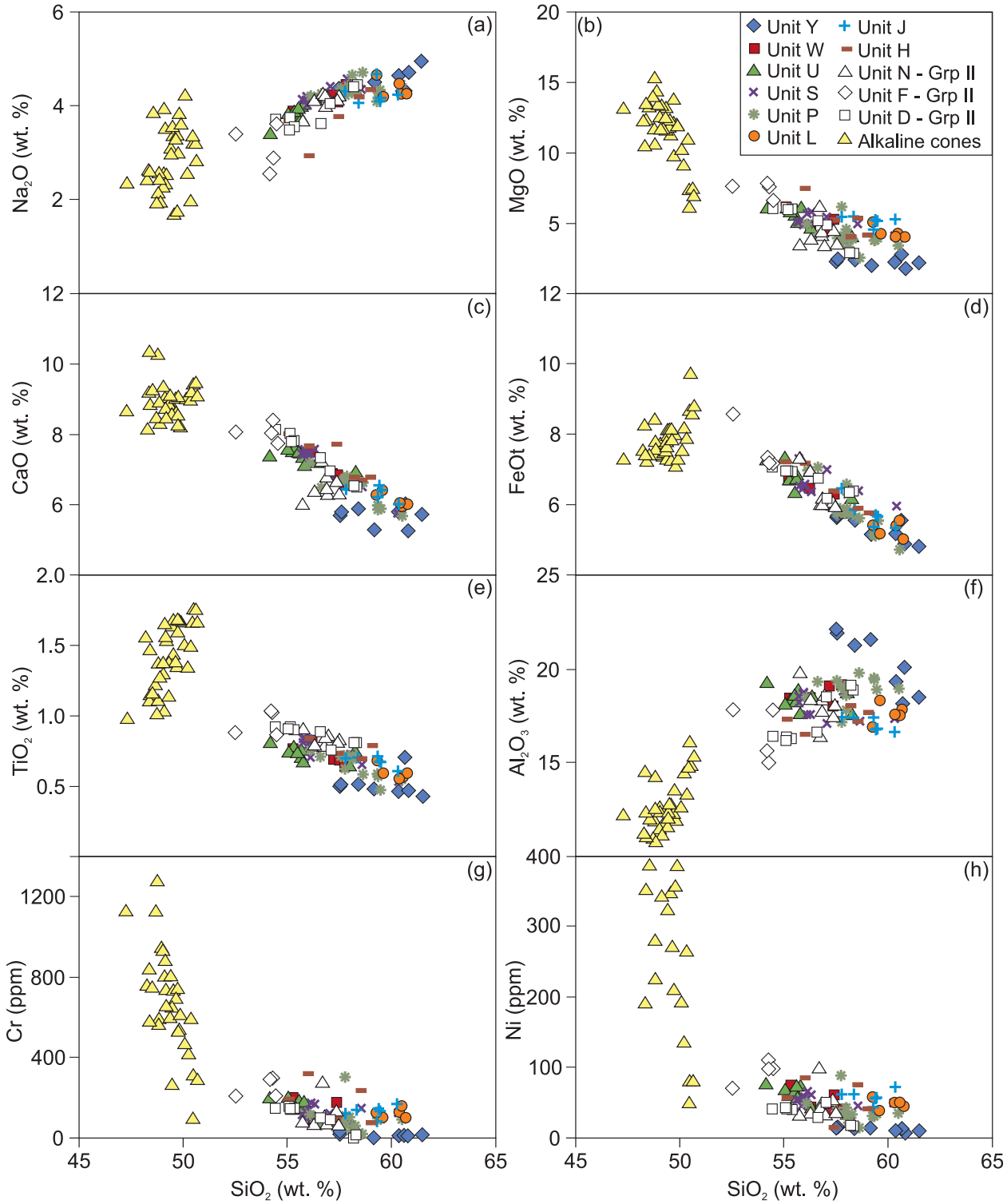

Fig. 6. Whole-rock major and compatible trace element variation diagrams for the CVC tephra fallout and alkaline cinder cone magmas. Geochemical data are reported in Table 3 and Supplementary Data Appendix 1.

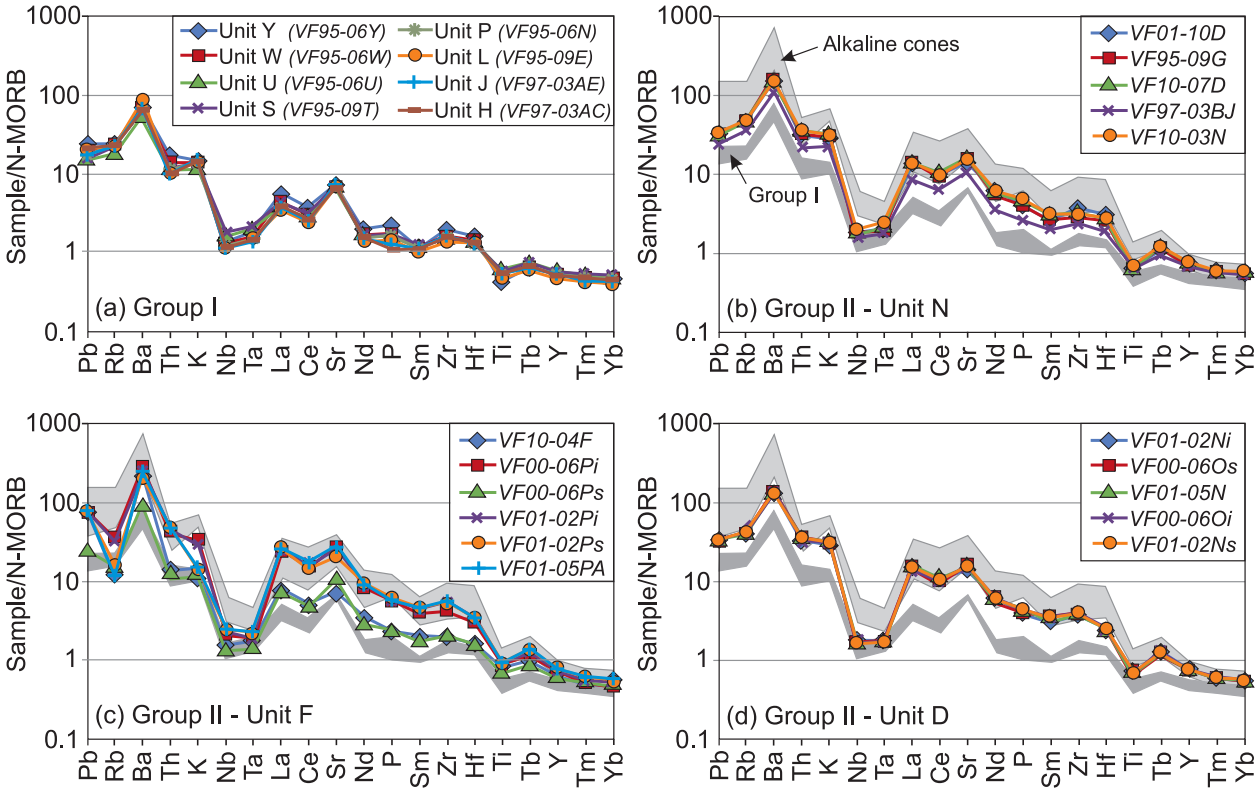

Fig. 7. N-MORB normalized incompatible trace element patterns for (a) the Group I tephra, and the Group II deposits, unit N (b), unit F (c) and unit D (d). N-MORB normalizing values are from Sun & McDonough (1989). The shaded areas represent the alkaline cinder cone magmas and the Group I eruption deposits. The data are reported in Table 4 and Supplementary Data Appendix 1.

glomerocrysts are present in all the samples (up to 2 vol. %), comprising plagioclase, clinopyroxene, orthopyroxene and commonly olivine and amphibole. The size of these varies from <1 mm to 5 mm.

Scoria from the Group II (high-K mafic) eruption deposits are basaltic andesite to trachyandesite in composition with phenocrysts and microphenocrysts of plagioclase + clinopyroxene + amphibole + olivine + phlogopite + Fe–Ti oxides in varying amounts (Table 6). The groundmass typically comprises dark, highly vesiculated glass, and contains abundant microlites of all the above phenocryst phases except amphibole. All three units (N, F and D) also contain up to 1 vol. % glomerocrysts of predominantly clinopyroxene and olivine and, less commonly, of orthopyroxene and phlogopite. The Group II units are mineralogically distinct from each other: unit N phenocrysts comprise predominantly plagioclase and clinopyroxene, with up to 1 vol. % olivine, and trace amounts of amphibole and phlogopite; scoria from unit F has a lower crystallinity (7–12 vol. %) than units N and D, and a mineral assemblage dominated by clinopyroxene, olivine and phlogopite with up to 1 vol. % plagioclase and trace amphibole, whereas unit D scoria has the highest crystallinity (10–15 vol. %; Table 6) comprising predominantly amphibole and plagioclase, with some clinopyroxene and up to 1 vol. % olivine and phlogopite.

Luhr & Carmichael (1981) described the alkaline cinder cone magmas as forming a transitional series from basanite to minette based on the appearance and increasing abundance of phlogopite, sanidine, leucite and apatite. The typical mineral assemblage of the basanites, as defined by Luhr & Carmichael (1981), comprises phenocrysts and microphenocrysts of olivine + clinopyroxene + (rare) plagioclase (labradorite $An_{50–70}$) + titanomagnetite within a crystalline groundmass glass comprising the same mineral phases. Leucite-basanites have the characteristic mineral assemblage of olivine + clinopyroxene phenocrysts, and microphenocrysts and groundmass crystals of sanidine + leucite + titanomagnetite + apatite + phlogopite (Luhr & Carmichael, 1981). The minettes comprise phenocrysts of olivine + clinopyroxene + phlogopite + apatite and microphenocrysts (and groundmass crystals) of sanidine, leucite, titanomagnetite, apatite and phlogopite (Luhr & Carmichael, 1981). The crystallinity of scoria samples from the alkaline cinder cones varies from 15·9 to 32·3 vol. % (Luhr & Carmichael, 1981).

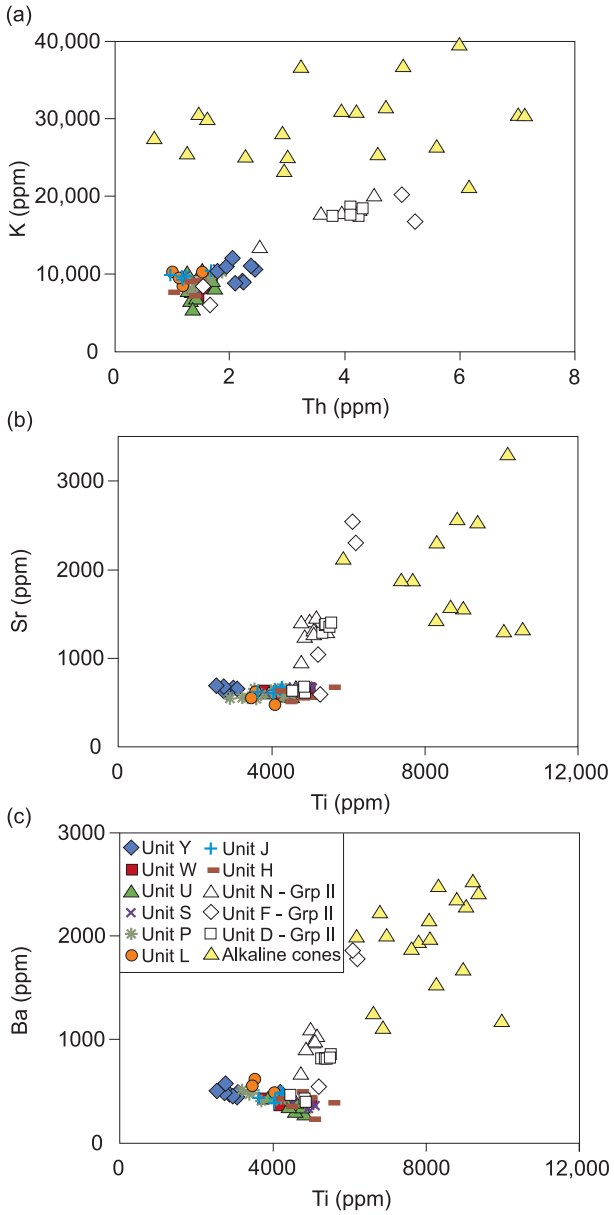

Fig. 8. Incompatible trace element variations highlighting the distinctions between the high-K (Group II) deposits and the Group I tephra. The majority of the Group II units display elevated K, Sr and Ba relative to the Group I deposits. One sample from unit N, two from unit F and three from unit D display K, Sr, and Ba concentrations similar to those of the Group I deposits. Ti is used in (b) and (c) as a proxy for Th, as an immobile element during secondary weathering processes, as some of the unit D samples have no ICP-MS data. (b) and (c) use XRF data. The data are reported in Tables 3 and 4.

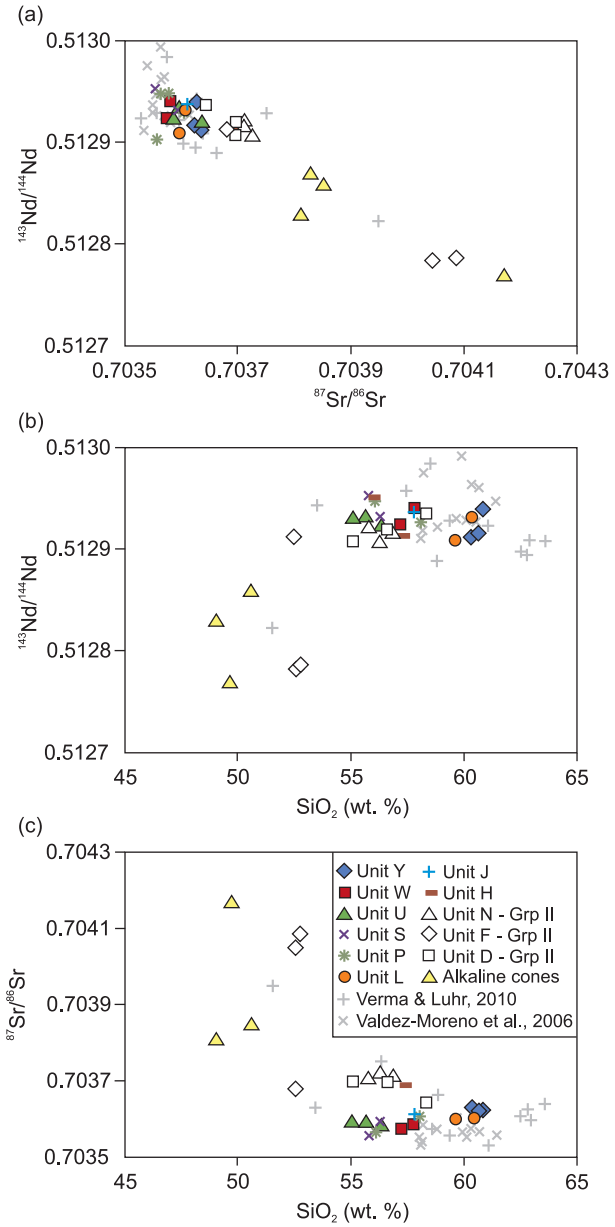

Fig. 9. (a) $^{87}Sr/^{86}Sr$ vs $^{143}Nd/^{144}Nd$, (b) $^{143}Nd/^{144}Nd$ and (c) $^{87}Sr/^{86}Sr$ variation with SiO_2 for the CVC eruption deposits. The majority of the Group II tephra have slightly more radiogenic $^{87}Sr/^{86}Sr$ and less radiogenic $^{143}Nd/^{144}Nd$ than the Group I deposits. However, two unit F samples display much more radiogenic $^{87}Sr/^{86}Sr$ and less radiogenic $^{143}Nd/^{144}Nd$ ratios than the rest of the CVC tephra. Isotopic data for the Group I and II deposits and the alkaline cinder cone magmas are reported in Table 5.

Mineral chemistry and textural characteristics

Plagioclase

Plagioclase is the dominant mineral phase in the Group I tephra samples, forming 2–15 vol. %, occurring as euhedral to subhedral microphenocrysts (<0·3 mm) and phenocrysts up to 3 mm in length (Fig. 10). The abundance of plagioclase in Group II tephra, however, varies between units, from trace amounts in unit F to 10 vol. % in unit N (Table 6). Plagioclase phenocrysts in Group II scoria are typically euhedral to subhedral and up to 2 mm

Table 6: Mineralogy of scoria from the Group II tephra fallout deposits observed at the CVC

Unit	Crystallinity	Plag	Cpx	Opx	Hbd	Olivine	Phlogopite	Fe–Ti oxides
Y	10–15	5–10	0–trace	0–trace	2–4	–	–	Trace–1
W	13–19	7–10	1–3	1–2	2–5	Trace–1	–	1
U	20–25	12–15	3–4	1–2	2–5	1–2	–	1
S	12–17	7–10	1–2	1	1–3	1–2	–	1
P	14–22	10–15	1–3	1–2	Trace	Trace	–	1
N	**9–13**	**5–10**	**1–2**	–	**Trace**	**Trace–1**	**Trace**	**1**
L	11–19	5–10	1	Trace	3–5	–	–	1–2
J	11–16	7–10	1–2	1	1	–	–	1–2
H	13–17	2–10	2–3	1–2	Trace–5	Trace–2	–	1
F	**7–12**	**Trace–1**	**2–5**	–	**Trace**	**1–3**	**1–2**	**1–2**
D	**10–15**	**1–3**	**Trace–2**	–	**3–7**	**Trace–1**	**1**	**1–3**

The Group II deposits are in bold. Crystallinity and abundances are given in volume % and were estimated from thin sections on the optical microscope. Plag, plagioclase; Cpx, clinopyroxene; Opx, orthopyroxene; Hbd, hornblende.

in length. The Group II scoria have a high plagioclase microphenocryst population relative to phenocrysts. Microphenocrysts are euhedral and appear to be unaltered.

In all CVC tephra samples (Group I and Group II), plagioclase phenocryst core and rim compositions display large variations in anorthite (An) content with core compositions ranging from An_{28} to An_{84} and rim compositions ranging from An_{24} to An_{83} (Table 7). Single plagioclase phenocrysts in all samples can show large variations in their core and rim An contents (up to 20 mol %; Fig. 10). These compositional variations are reflected in the mineral textures. Several types of plagioclase phenocryst are observed in the Group I and Group II deposits displaying sieve textures, normal zoning, reverse zoning, oscillatory zoning and combinations of these with dissolution surfaces and resorption textures (Fig. 10). Sieve-textured plagioclase is common in samples from both groups (Fig. 10a and b). These phenocrysts have undergone pervasive resorption, leaving a porous, sieve texture, which was infilled by melt, and has undergoine subsequent recrystallization giving the crystals a patchy appearance (Fig. 10b). The An content varies by up to 30 mol % between the light and dark patches. Phenocrysts displaying oscillatory zoning are also common, with both large-scale, sawtooth oscillations (up to 100 μm width and 20 mol % An amplitude) and fine low-amplitude oscillations (Fig. 10c–e). Core–rim EPMA analyses reveal that compositional changes in An content are commonly coincident with changes in Fe_2O_3 (Fig. 10d and e).

Clinopyroxene

Clinopyroxene (augite) is present in all Group I and Group II tephra, varying in abundance from trace amounts to 5 vol. % and commonly occurring as pairs of crystals or in glomerocrysts (Table 6). Crystals are typically ~0·5 mm across, but can be up to 1·5 mm, and are euhedral to subhedral.

All clinopyroxene phenocrysts display core–rim chemical variations reflected in their Mg#. Clinopyroxene phenocrysts in tephra from the majority of the Group I subalkaline deposits have cores with Mg# varying from 0·73 to 0·83 and rims with Mg# varying from 0·74 to 0·84 (Table 7). Tephra from the most mafic of the Group I units (U and H) contains clinopyroxene phenocrysts with cores with Mg# up to 0·88. Within the Group II samples, core compositions are typically more magnesian than the Group I clinopyroxene cores, with Mg# of up to 0·90 (Table 7). Rims are similar in composition to the Group I clinopyroxenes, with Mg# ranging from 0·72 to 0·85.

Clinopyroxene phenocrysts in all samples are typically subhedral displaying embayed edges. They exhibit complex dissolution, resorption and recrystallization textures including rounded and embayed growth zones, dissolution surfaces cross-cutting multiple growth zones and patchy sieve textures (Figs 11 and 12). Zoning is common in all phenocrysts of normal, reverse and oscillatory types (Figs 11 and 12). Resorption and dissolution surfaces are commonly surrounded by growth zones displaying large changes in Mg# coinciding with changes in Cr_2O_3 (Figs 11 and 12). Figure 11a shows a clinopyroxene phenocryst (sample VF95-09L, unit P) from Group I with a low-Mg core (Mg# 0·79), which is partially resorbed, surrounded by a high-Mg growth zone (Mg# 0·86), and oscillatory growth to the rim. The high-Mg growth zone is coincident with a large step increase in Cr_2O_3 (Fig. 11a). Similarly, Fig. 11b displays a clinopyroxene phenocryst

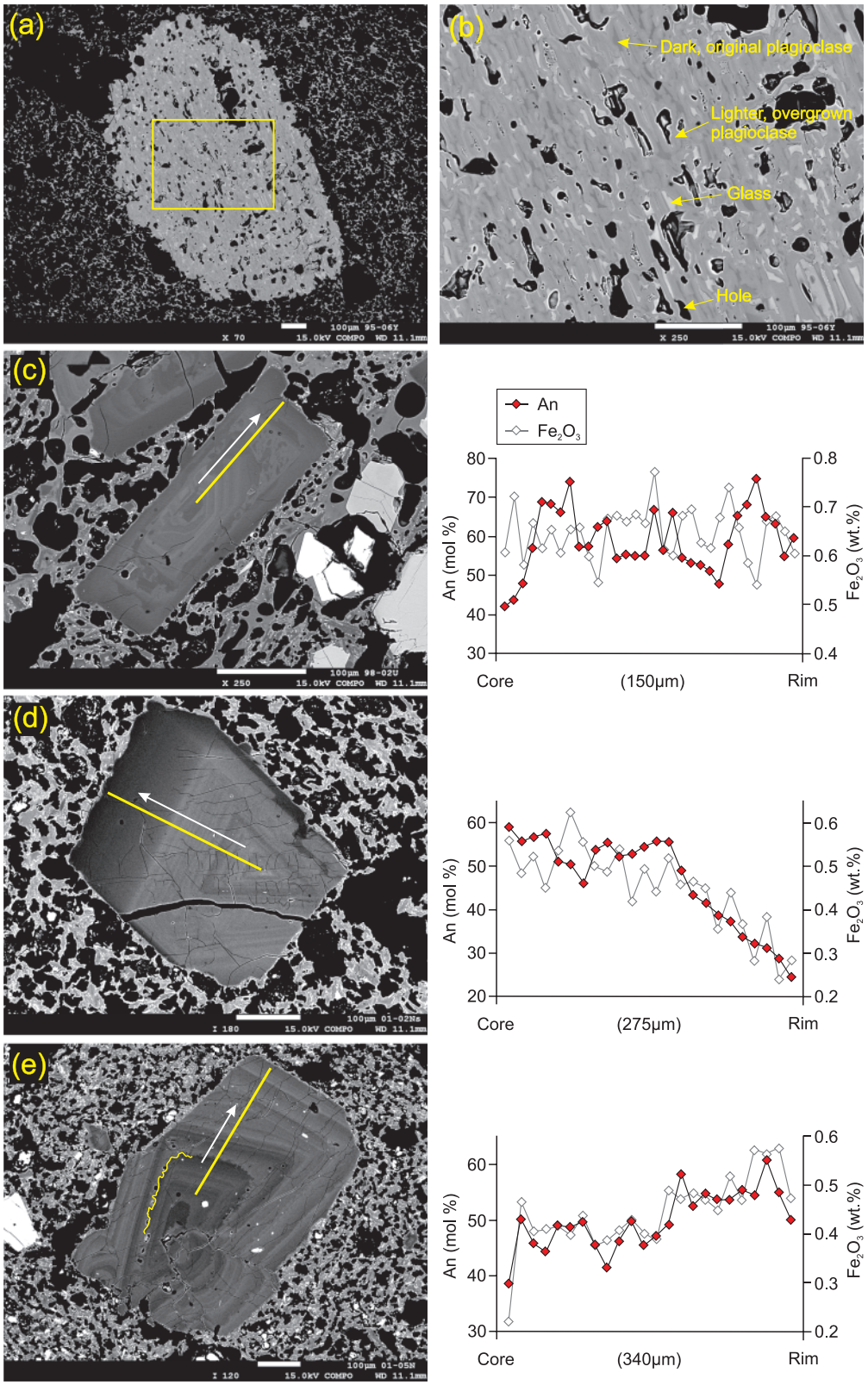

Fig. 10. Backscatter SEM images for plagioclases from units Y (a and b; sample VF95-06Y) and U (c; sample VF98-02U) of the Group I deposits, and unit D (d and e; samples VF0l-02Ns and VF0l-05N, respectively) of the Group II deposits. Core–rim EPMA profiles are also shown for (c), (d) and (e). Errors are within the symbol size. Sieve-textured plagioclase (a and b) is common in both Group I and II tephra samples. The majority of plagioclase phenocrysts in all tephra samples display complex zoning, with changes in An composition reflected in Fe_2O_3 (c–e). The core–rim EPMA data are reported in the Supplementary Data, Appendix 3.

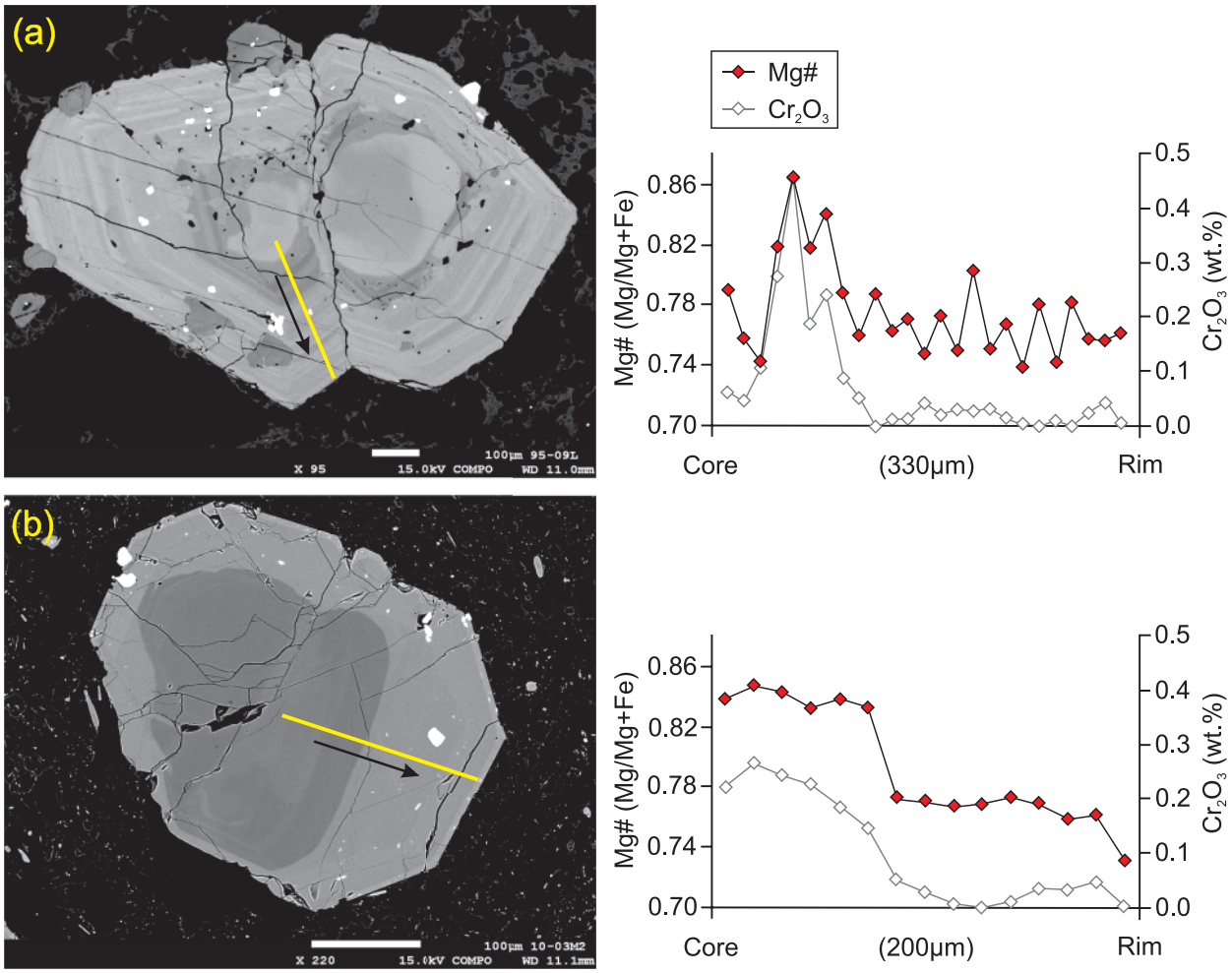

Fig. 11. Clinopyroxene phenocrysts from (a) unit P (sample VF95-09L) and (b) unit H (sample VFl0-03M2) of the Group I deposits. Also shown are core–rim profiles for (a) and (b). Errors are within the symbol size. Compositional changes in Mg# are typically coincident with equivalent changes in Cr_2O_3. The core–rim EPMA data are reported in the Supplementary Data, Appendix 3.

from the Group I tephra (VFl0-03M2, unit L) which has a rounded, high-Mg core (Mg# 0·84) surrounded by low-Mg (Mg# 0·78) growth to the rim. The step decrease in Mg# between the core and the surrounding growth zone is also coincident with a step decrease in Cr_2O_3.

Similar complex zoning patterns are displayed by clinopyroxene crystals in the Group II deposits. Figure 12a shows a clinopyroxene phenocryst (VF00-06O, unit D) with a sieve-textured, high-Mg core (Mg# 0·87) and a low-Mg overgrowth (Mg# 0·77). The sharp step decrease in Mg# is coincident with a decrease in Cr_2O_3. Clinopyroxenes with a low-Mg core (Mg# 0·73–0·74) that is resorbed and recrystallized are also common in the Group II samples (Fig. 12b and c; VF0l-05N and VF00-06O, unit D). Surrounding the patchy textured low-Mg core is a high-Mg zone (Mg# 0·85), overgrown by less magnesian clinopyroxene to the rim (Mg# 0·8l). Again, the step increase in Mg# is coincident with a step increase in Cr_2O_3. All zones display resorption textures with rounded crystal edges and corners.

Orthopyroxene

Orthopyroxene is present in all of the Group I eruption deposits, varying in abundance from trace to 2 vol. %, but is present in the Group II units only in glomerocrysts along with clinopyroxene, olivine and rarely, phlogopite. Phenocrysts display marked zoning and embayed rims, and, similar to clinopyroxene crystals, are commonly observed in crystal pairs or in glomerocrysts. Orthopyroxenes are enstatite-rich in composition with Mg# ranging from 0·69 to 0·85 in cores and from 0·69 to 0·8l in rims (Table 7).

The majority of the orthopyroxene phenocryst cores and growth zones display strong or partial resorption such as rounded corners and embayed crystal edges, sieve and patchy textures, and dissolution surfaces cross-cutting

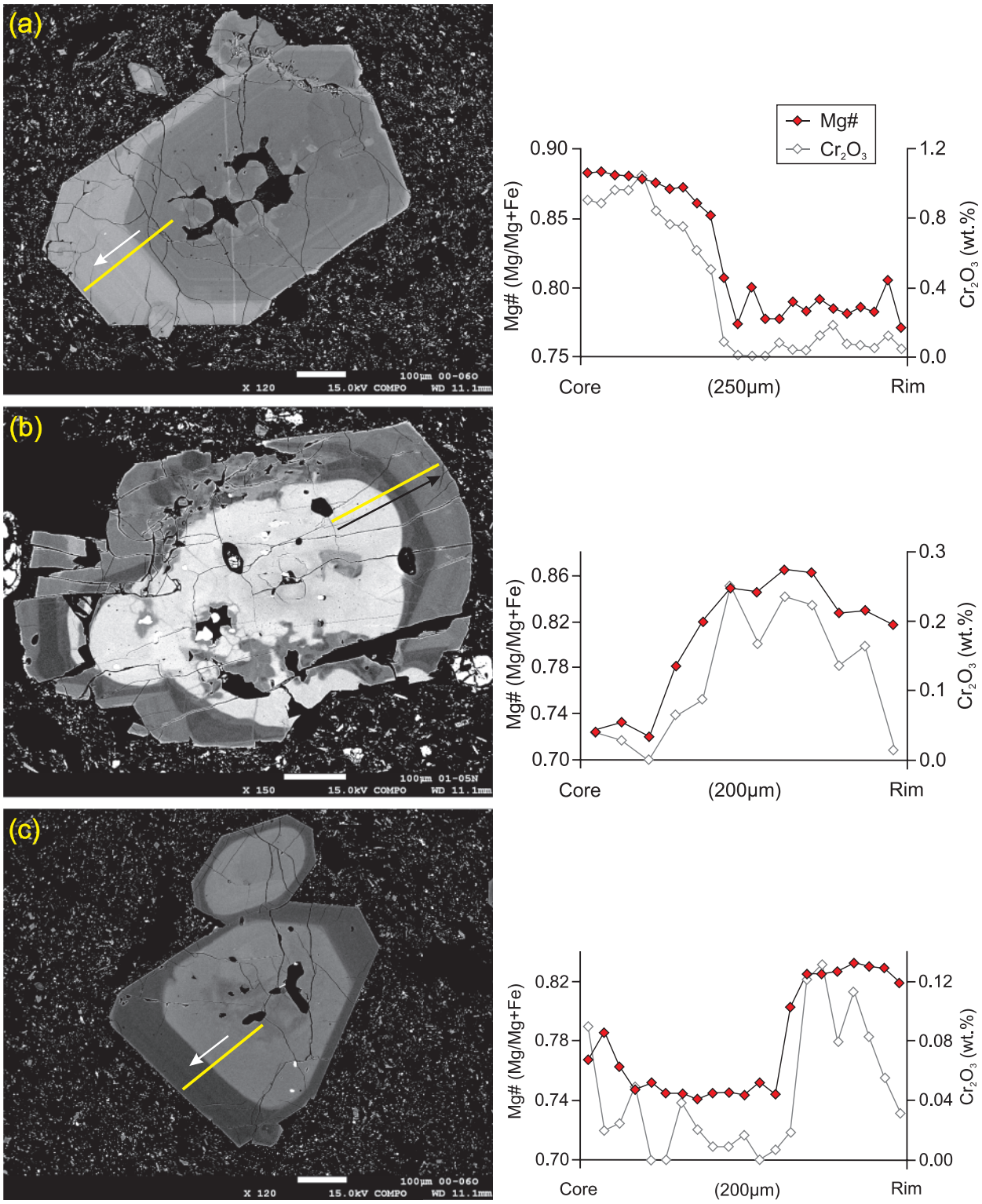

Fig. 12. Backscatter SEM images from unit D, samples VF00-06Oi (a, c) and VF0l-05N (b); and core–rim EPMA profiles of clinopyroxene phenocrysts from Group II. Errors are within the symbol size. Compositional changes in Mg# are typically coincident with equivalent changes in Cr_2O_3, as observed in the Group I clinopyroxene. The core–rim EPMA data are reported in the Supplementary Data, Appendix 3.

Table 7: Mineral chemistry of scoria from the medium-K Group I and high-K mafic Group II eruption deposits

	Medium-K Group I								
Unit	Glass SiO_2 (wt %)	Plagioclase An (mol.%)		Clinopyroxene Mg#		Orthopyroxene Mg#		Olivine Mg#	
	Average	Cores	Rims	Cores	Rims	Cores	Rims	Cores	Rims
Y	65·4	64	57						
	(*n* = 98; 54·2–74·0)	(*n* = 36; 28–83)	(*n* = 51; 29–83)	–	–	–	–	–	–
W	61·43	57	51	0·80	0·79	0·76	0·78	0·78	0·78
	(*n* = 37; 54·1–70·9)	(*n* = 14; 38–84)	(*n* = 13; 59–64)	(*n* = 8; 0·76–0·83)	(*n* = 7; 0·77–0·81)	(*n* = 4;0·75–0·77)	(*n* = 2;0·78)	(*n* = 17;0·76–0·80)	(*n* = 16;0·76–0·79)
U	60·4	61	59	0·80	0·79	0·76	0·77	0·76	0·77
	(*n* = 86; 56·5–70·1)	(*n* = 23; 42–80)	(*n* = 23; 41–79)	(*n* = 18; 0·75–0·87)	(*n* = 29;0·75–0·83)	(*n* = 13;0·69–0·80)	(*n* = 14;0·69–0·80)	(*n* = 17;0·72–0·78)	(*n* = 20; 0·72–0·78)
S	64·2	57	53	0·78	0·76	0·78	0·73		
	(*n* = 9; 57·8–72·7)	(*n* = 15; 51–69)	(*n* = 15; 46–58)	(*n* = 3;0·75–0·81)	(*n* = 3;0·75–0·77)	(*n* = 10;0·73–0·85)	(*n* = 11;0·71–0·75)	–	–
P	67·0	54	50	0·78	0·76	0·76	0·74		
	(*n* = 20;64·6–68·9)	(*n* = 9; 48–70)	(*n* = 20; 45–55)	(*n* = 6;0·76–0·79)	(*n* = 7;0·75–0·79)	(*n* = 6;0·73–0·79)	(*n* = 12;0·72–0·77)	–	–
L	71·8	64	53	0·75	0·84	0·78	0·73		
	(*n* = 37; 66·3–75·8)	(*n* = 15; 64–80)	(*n* = 16; 46–62)	(*n* = 6;0·73–0·77)	(*n* = 2; 0·84)	(*n* = 2;0·74–0·81)	(*n* = 4;0·71–0·73)	–	–
J	62·5	56	53	0·78	0·79	0·83	0·77		
	(*n* = 25; 54·5–68·6)	(*n* = 15; 43–71)	(*n* = 14; 39–71)	(*n* = 7;0·76–0·80)	(*n* = 13;0·75–0·84)	(*n* = 3;0·78–0·85)	(*n* = 12;0·72–0·81)	–	–
H	61·2	47	52	0·83	0·77	0·72	0·77	0·83	0·79
	(*n* = 31; 57·2–70·6)	(*n* = 18; 31–69)	(*n* = 17; 37–70)	(*n* = 16;0·76–0·88)	(*n* = 15;0·74–0·83)	(*n* = 6;0·69–0·75)	(*n* = 7;0·74–0·81)	(*n* = 9;0·80–0·87)	(*n* = 8;0·77–0·83)

	High-K mafic Group II							
Unit	Glass SiO_2 (wt %)	Plagioclase An (mol %)		Clinopyroxene Mg#		Olivine Mg#		Phlogopite Mg#
	Average	Cores	Rims	Cores	Rims	Cores	Rims	Average
N	59·1	57	56	0·81	0·80	0·80	0·79	
	(*n* = 55; 54·6–64·9)	(*n* = 12; 53–64)	(*n* = 25; 47–65)	(*n* = 12; 0·74–0·89)	(*n* = 21; 0·72–0·82)	(*n* = 8; 0·77–0·80)	(*n* = 10; 0·77–0·80)	–
F	58·5	52	52	0·83	0·81	0·87	0·81	0·81
	(*n* = 5; 56·8–59·1)	(*n* = 11; 42–62)	(*n* = 10; 44–59)	(*n* = 25; 0·70–0·90)	(*n* = 22; 0·73–0·85)	(*n* = 8; 0·86–0·88)	(*n* = 9; 0·79–0·82)	(*n* = 47; 0·76–0·82)
D	59·2	54	46	0·82	0·81	0·86	0·79	
	(*n* = 41; 54·4–65·6)	(*n* = 33; 34–78)	(*n* = 22; 24–74)	(*n* = 37; 0·72–0·88)	(*n* = 25; 0·75–0·83)	(*n* = 14; 0·85–0·87)	(*n* = 13; 0·79–0·81)	–

For each mineral, the average composition is given in the first row, with the number of analyses and the range of compositions in the second row.

multiple growth zones (Fig. 13). As observed in the clinopyroxene phenocrysts, large step increases and decreases in Mg# are typically coincident with changes in Cr_2O_3 (Fig. 13).

Amphibole

Amphiboles are magnesiohastingsite in composition (Leake *et al.*, 1997), occurring as phenocrysts and/or microphenocrysts in all of the CVC eruption deposits. Abundances in the Group I deposits range from <1 to 5 vol. %, whereas amphibole in the Group II deposits varies from trace amounts in units N and F to between 3 and 7 vol. % in unit D (Table 6).

Amphibole in the Group I eruption deposits occurs as euhedral to subhedral phenocrysts with a prismatic habit, typically up to 1·5 mm in length. They commonly appear broken, and rims are generally sharp; however, hornblende phenocrysts with strong reaction rims of pyroxene, plagioclase and Fe–Ti oxides are present in all units. Ghost hornblende, having completely altered to oxides, pyroxene and plagioclase, is rare but does occur. Both altered and fresh crystals occur together in units S and L of Group I.

Amphibole phenocrysts in unit D are typically up to 2 mm in length and are subhedral with rounded edges. Pyroxene, plagioclase and Fe–Ti oxide reaction rims surrounding the amphiboles are rare; however, holes in the centre are common and many phenocrysts appear broken (Fig. 14a and b). Amphibole in units N and F occurs as anhedral microphenocrysts.

Olivine

Olivine is present in all Group I eruption deposits except the more evolved units Y and L, and the intermediate unit J (Table 6). Its abundance varies from trace amounts to 2 vol. %, and it occurs as rounded and embayed phenocrysts up to 1 mm across and as microphenocrysts. Olivine is more common in all three of the Group II units (up to 3 vol. %), forming rounded and embayed phenocrysts up to 1 mm across and microphenocrysts (Fig. 14c).

Core and rim Mg# values of olivine phenocrysts from the Group I scoria typically display small variations, ranging from 0·72 to 0·80 in cores and in rims (units W and U; Table 7). Olivine phenocrysts from unit H are more magnesian with Mg# 0·80–0·87 in cores and 0·77–0·83 in rims. Olivine phenocrysts within the Group II eruption deposits are typically more magnesian with Mg# of up to 0·88 (Table 7). The core and rim Mg# values of the olivines do not display large variations; for example, unit D cores have Mg# of 0·85–0·87 and rims have 0·79–0·81. Weak zonation from core to rim is common, with less magnesian rims (Fig. 14c). Olivine is also common in glomerocrysts, where it occurs together with clinopyroxene and, less commonly, orthopyroxene and phlogopite.

Phlogopite

One of the diagnostic charateristics of the Group II eruption deposits is the presence of phlogopite microphenocrysts and/or phenocrysts. Phlogopite varies in abundance from trace amounts in unit N to 2 vol. % in unit F (Table 6). It occurs as microphenocrysts in units N and D, and as up to 1 mm long phenocrysts in unit F (Fig. 14d). Phlogopite also occurs in glomerocrysts together with clinopyroxene, olivine ± orthopyroxene. Phenocrysts and microphenocrysts display very little compositional variation, with Mg# ranging from 0·76 to 0·82 (Table 7).

Fe–Ti oxides

Fe–Ti oxides, including both titanomagnetite and ilmenite, are common in the groundmass of all the CVC eruption deposits, with abundances varying from ~1 to 3 vol. % (Table 6). Unit D of Group II has the highest abundance. Fe–Ti oxides are also common in glomerocrysts and as inclusions in olivine and clinopyroxene crystals. The breakdown rims of amphibole phenocrysts also contain Fe–Ti oxides.

Accessory minerals

The only accessory mineral observed in the CVC tephra is apatite, which occurs as small euhedral (<30 μm) inclusions in amphibole phenocrysts and as microphenocrysts in the groundmass in Group I and Group II tephra. Luhr & Carmichael (1982) also reported spinel inclusions in olivine and in the groundmass of scoria samples.

Groundmass

The groundmass of the Group I pumice and scoria typically comprises intermediate to felsic glass (54·1–75·8 wt % SiO_2; Fig. 14e, Table 7) with abundant microlites of plagioclase and pyroxene. Pumice and scoria clasts commonly display colour variations reflecting heterogeneity of the glass, with up to 20 wt % variation in SiO_2 content within a single pumice clast.

The groundmass of the Group II scoria is less evolved, typically comprising intermediate to felsic glass ranging in composition from 54·4 to 65·6 wt % SiO_2 (Fig. 14e; Table 7). Units N and D show the widest range of glass SiO_2 contents, with variations of up to 11 wt % (Table 7; Fig. 14e) and a distinctly streaky appearance. In contrast, the groundmass glass of unit F scoria shows very little variation in SiO_2 (56·8–59·1 wt %) and does not have a streaky appearance. These variations in glass chemistry are also reflected in the TiO_2 and MgO concentrations (not shown). The groundmass is typically highly vesiculated and contains abundant microlites of plagioclase and clinopyroxene (Fig. 14f).

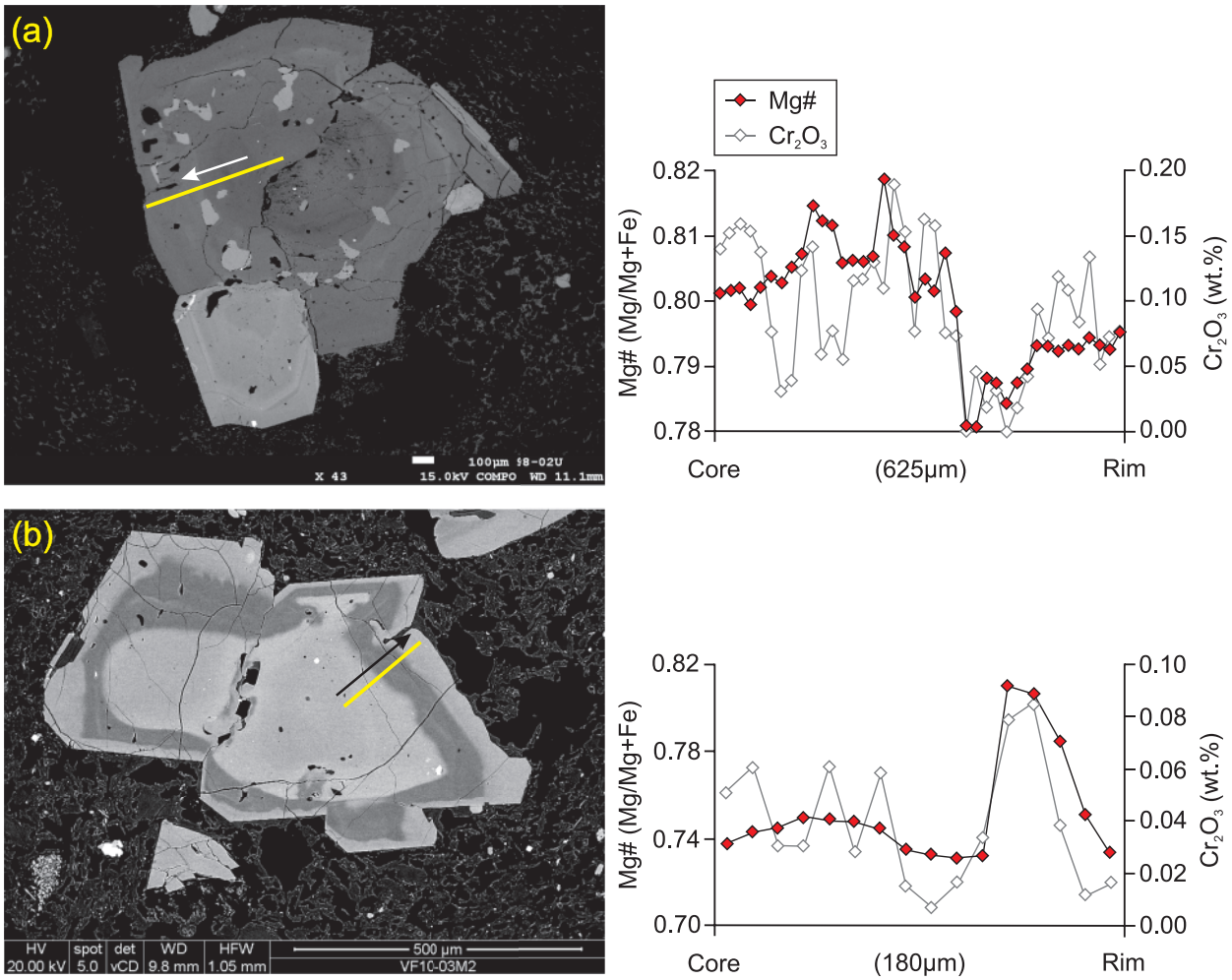

Fig. 13. Backscatter SEM images and EPMA core–rim profiles of orthopyroxene phenocrysts from Group I, samples VF98-02U from unit N (a) and VF10-03M2 from unit L (b). Errors are within the symbol size. The SEM images and EPMA data reveal complex zoning patterns and coincident compositional changes in Mg# and Cr_2O_3. The core–rim EPMA data are reported in the Supplementary Data, Appendix 3.

DISCUSSION

Magma mingling

Geochemical similarities between subalkaline and alkaline magmas

The whole-rock major and trace element geochemical data reveal that the high-K Group II units, N, F and D, have elevated K_2O, P_2O_5 and fluid-mobile incompatible element contents that trend towards the shoshonitic alkaline cinder cone magma compositions and away from the Group I, medium-K subalkaline compositions (Figs 4, 6 and 7).

The variation of K_2O and P_2O_5 with SiO_2 for the CVC eruptive products shows that the high-K Group II eruption deposits are compositionally intermediate between the medium-K Group I and the high-K alkaline cinder cone magmas (Fig. 4b and c). The subalkaline and alkaline magmas define separate differentiation trends, and therefore cannot be linked through fractional crystallization from a common evolving parental melt. Two-component mixing calculations between the most primitive and most evolved Group I subalkaline magma compositions and the most K-rich alkaline cinder cone magma suggest that the Group II eruption deposits could contain large amounts (up to 50%) of the alkaline magma component (Fig. 15). The least and most evolved Group I samples (VF01-01T from unit U and VF97-05B from unit L), and a high-K minette sample (LE-02; Vigouroux *et al.*, 2008) from La Erita cinder cone were used as end-member compositions (Table 8).

The presence of an alkaline magma component in the Group II magmas can also be shown through simple mixing calculations using the whole-rock trace element variations (Fig. 16; Table 9). As previously discussed, the incompatible trace element patterns of the Group II deposits overlap those of the high-K alkaline cinder cone magmas.

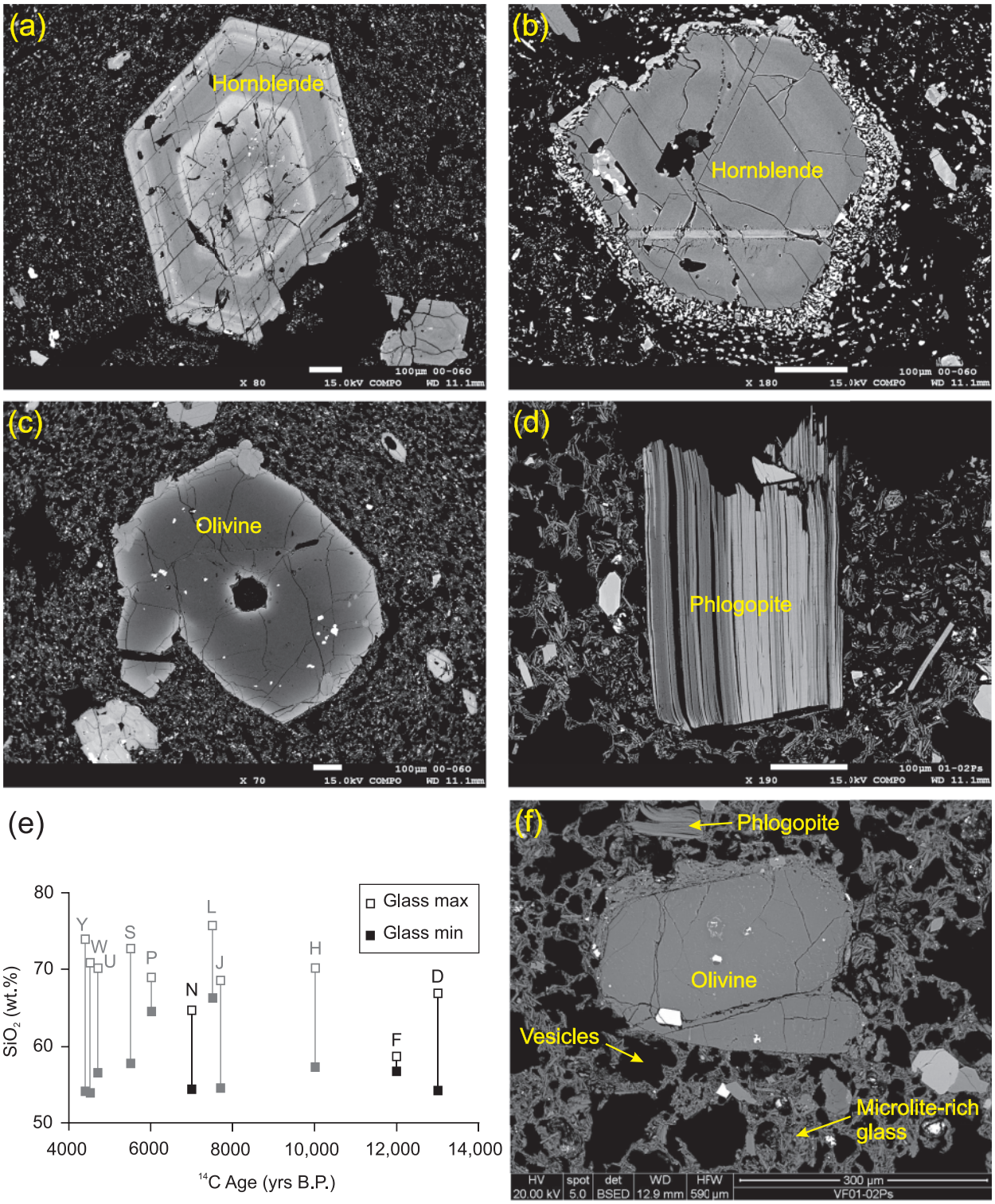

Fig. 14. Backscatter SEM images of (a, b) hornblende, (c) olivine, (d) phlogopite and (f) groundmass glass. Images (a)–(c) are from sample VF00-06O from unit D, and (d) and (f) are from unit F, sample VF01-02Ps. (e) is a plot showing the variation in groundmass glass SiO_2 content in the Group I (grey) and Group II (black) units. Errors are within the symbol size. The range of glass SiO_2 data is reported in Table 7. The groundmass is typically more heterogeneous and evolved in the Group I tephra than in the Group II tephra.

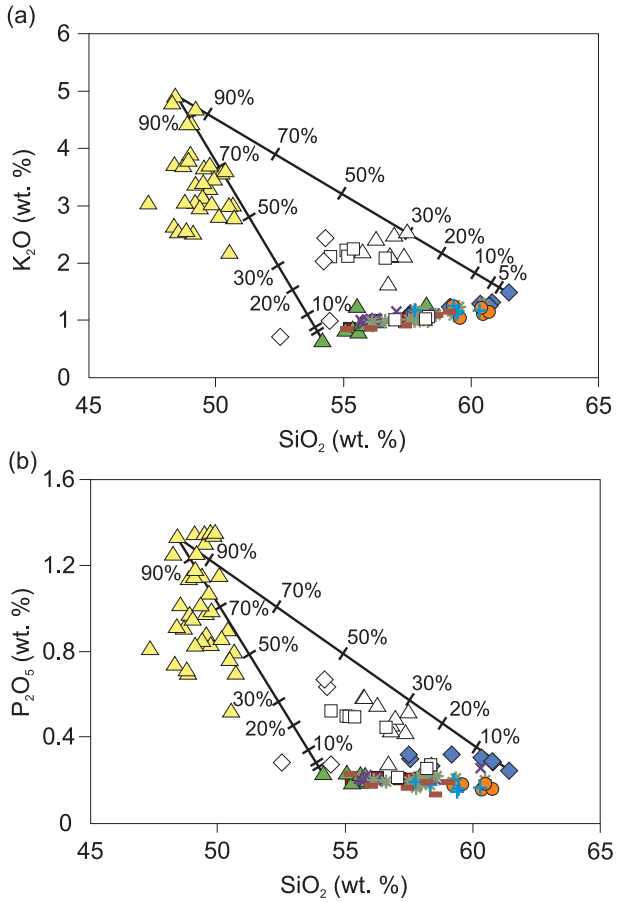

Fig. 15. Whole-rock major element K_2O (a) and P_2O_5 (b) variation with SiO_2 showing mixing lines between end-member compositions after Langmuir *et al.* (1978). The subalkaline end-members are the least and most evolved Group I samples (VF01-01T from unit U and VF97-05B from unit L), and the alkaline end-member is a high-K minette sample (LE-02; Vigouroux *et al.*, 2008) from La Erita cinder cone (Table 8). The Group II deposits lie compositionally between the Group I and alkaline cinder cone magmas, with potentially up to 50% alkaline magma component.

Table 8: End-member compositions used in mixing calculations in Fig. 15

Sample:	VF01-01T*	VF97-05B*	LE-02*
Unit:	U	Y	Cinder cone
Age (a BP):	4700	4400	–
Reference:	1	1	2
SiO_2	54·17	61·47	48·41
TiO_2	0·81	0·43	1·47
Al_2O_3	19·36	18·47	11·10
FeOt	7·27	4·79	7·27
MnO	0·12	0·10	0·12
MgO	6·09	2·16	12·40
CaO	7·38	5·70	8·88
Na_2O	3·41	4·95	2·55
K_2O	0·67	1·48	4·94
P_2O_5	0·24	0·24	1·34
Total	100	100	100

References: 1, Luhr *et al.* (2010); 2, Vigouroux *et al.* (2008).
*Samples VF01-01T from unit U and VF97-05B from unit Y are the least and most evolved end-members from the Group I subalkaline samples; sample LE-02 from La Erita cinder cone (Vigouroux *et al.*, 2008) was used for the alkaline end-member, with the highest whole-rock K_2O content.

The trace element abundance patterns for calculated mixed magma compositions (5%, 20% and 50% alkaline component) broadly match those of the Group II deposits (Fig. 16). They do not agree perfectly, however. For example, the abundances representing a 50:50 alkaline–subalkaline mixture agree well for the majority of trace elements with the exception of Rb, Ba, Nb, P, Zr and Hf, which are all more enriched than in the Group II samples. This may reflect the presence of small amounts of accessory minerals in the alkaline melts, such as titanite, rutile, zircon or apatite, which would result in relatively high abundances of Nb, P, Zr and Hf (Cox *et al.*, 1979; Pearce, 1982; Saunders *et al.*, 1991). Rb and Ba are highly mobile in fluids, therefore intense source metasomatism can cause enrichments in the alkaline mixing endmember (e.g. the Catalina Schist Mélange, Bebout & Barton, 1989; Papua

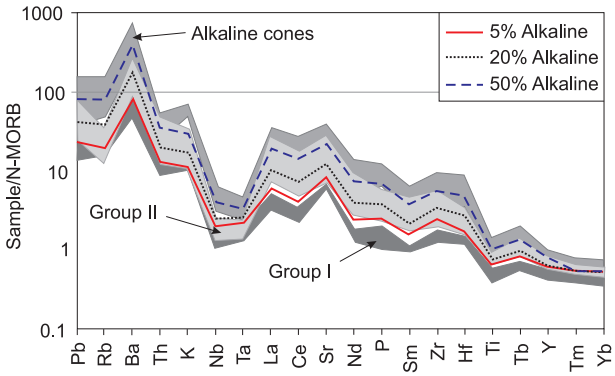

Fig. 16. N-MORB normalized incompatible trace element abundance diagram showing trace element patterns produced by mixing between the subalkaline and alkaline magmas. The mixed compositions are calculated using a representative basaltic andesite from Group I (VF01-01T) and an alkaline minette (SAY-7E from El Carpintero Norte cinder cone; Cai, 2009; Table 9). The continuous red line represents compositions consisting of a mixture 95% subalkaline and 5% alkaline magma; the black dotted line represents 20% alkaline magma; the purple dashed line is a 50% alkaline–subalkaline mixture. The Group II magmas (light grey field) have between 20 and 50% alkaline component. N-MORB normalizing values are from Sun & McDonough (1989).

Table 9: End-member compositions used in trace element mixing calculations in Fig. 16

Sample:	VF01-01T*	SAY-7E*
Unit:	U	Cinder cone
Age (a BP):	4700	–
Reference:	1	2
Rb	7·1	82·2
Ba	290	4657
Th	1·35	7·00
K	5542	29718
Nb	4·14	14·18
Ta	0·28	0·58
La	11·16	84·21
Ce	22·94	194·4
Sr	602	3327
Nd	13·85	94·75
P	1031	5761
Sm	3·51	15·83
Zr	104	682
Hf	2·93	17·13
Ti	4861	9832
Tb	0·53	1·33
Y	17·19	26·88
Tm	0·26	0·23†
Yb	1·60	1·79

References: 1, Luhr *et al*. (2010); 2, Cai (2009).
*Sample VF01-01T from unit U is used as a representative basaltic andesite end-member; sample SAY-7E is the most enriched of the alkaline cinder cone samples and is therefore used as the alkaline magma end-member.
†There are no Tm data for SAY-7E, therefore Tm was taken from a representative minette from San Isidro cinder cone, sample VF99-07A (Maria & Luhr, 2008).

New Guinea, McInnes *et al*., 2001; Izu–Bonin–Mariana arc–basin system, Savov *et al*., 2007; Kamchatka arc xenoliths, Halama *et al*., 2009). Alternatively, a low degree of partial melting could result in high concentrations of Rb and Ba in the melt.

The alkaline–subalkaline magma mixing relationship can also be explored by consideration of the $^{87}Sr/^{86}Sr$ and $^{143}Nd/^{144}Nd$ isotope variations within Groups I and II. Again, the Group II tephra compositions trend towards those of the alkaline cinder cone magmas. The majority of the Group II samples are isotopically similar to the Group I medium-K subalkaline series; however, two unit F samples have distinctly more radiogenic $^{87}Sr/^{86}Sr$ and less radiogenic $^{143}Nd/^{144}Nd$ than the rest of the CVC tephra samples (Fig. 9). Using two-component mixing calculations, the majority of the Group II eruption deposits are shown to fall

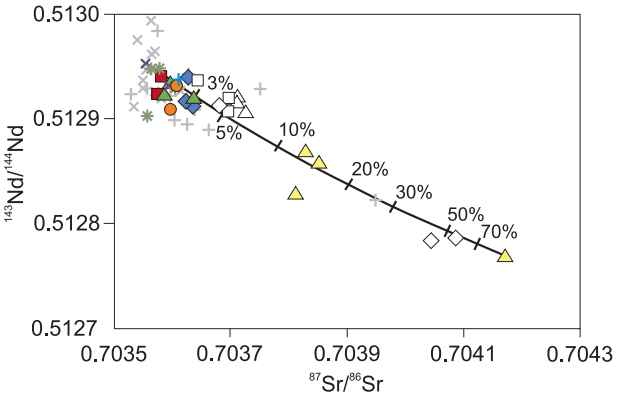

Fig. 17. Two-component mixing line between the end-member magmas on a $^{87}Sr/^{86}Sr$ vs $^{143}Nd/^{144}Nd$ plot using end-member compositions of a Group I basaltic andesite with the most radiogenic $^{143}Nd/^{144}Nd$ (sample VF95-06P) and an alkaline cinder cone minette with the most radiogenic $^{87}Sr/^{86}Sr$ and least radiogenic $^{147}Nd/^{146}Nd$ (sample SAY-7E from El Carpintero Norte; Cai, 2009; Table 10). The tick marks show the percentage of the alkaline component. The majority of the Group II samples have around 5% alkaline component whereas the two unit F samples VF01-02Ps and VF01-05PA have up to 50% of the alkaline component.

Table 10: Whole-rock isotopic data used in mixing calculations in Fig. 17

Sample:	VF95-06P	SAY-7E
Unit:	S	Cinder cone
Reference:	1	2
Sr (ppm)	639	3327
Nd (ppm)	13·66	94·75
$^{87}Sr/^{86}Sr$	0·70355	0·70417
$^{143}Nd/^{144}Nd$	0·51295	0·51277

References: 1, Luhr *et al*. (2010); 2, Cai (2009).
*Sample VF95-06P from unit S is used as a representative basaltic andesite Group I end-member with the most radiogenic $^{143}Nd/^{144}Nd$; sample SAY-7E is the alkaline end-member with the most radiogenic $^{87}Sr/^{86}Sr$ and least radiogenic $^{147}Nd/^{146}Nd$.

along a mixing line involving up to 5% of the alkaline magma component, whereas the two unit F samples have ~50% of the alkaline cinder cone component (Fig. 17; Table 10). The range of variation in the cinder cone magmas could equally be explained by mixing with a subalkaline component similar to a typical Group I magma.

Mineralogical similarities between subalkaline and alkaline magmas

The Group II tephra deposits are basaltic andesites, yet are characterized by mineral assemblages including

clinopyroxene, olivine and phlogopite, more akin to those of the basanites and minettes of the alkaline cinder cones (Luhr & Carmichael, 1981). In the alkaline cinder cone magmas, plagioclase is absent, or present only in the groundmass (Luhr & Carmichael, 1981). Geochemically, unit F of Group II shows the strongest alkaline signature (Figs 15 and 17), consistent with its mineralogy, which comprises an assemblage dominated by clinopyroxene, olivine and phlogopite with minor plagioclase and a trace amount of amphibole (Table 6). Units N and D have weaker alkaline signatures, which, again, are reflected in their mineralogy; unit N scoria comprises predominantly plagioclase and clinopyroxene, with up to 1 vol. % olivine, and trace amounts of amphibole and phlogopite, whereas Unit D scoria comprise predominantly amphibole and plagioclase, with clinopyroxene and up to 1 vol. % olivine and phlogopite. The Group I tephra samples comprise predominantly plagioclase, clinopyroxene, orthopyroxene and hornblende with olivine in the more mafic units. These mineralogical differences, together with the geochemical data, suggest that the Group II tephra resulted from mixing between alkaline and subalkaline magmas at a late stage in the eruption process, producing magma with an overall subalkaline whole-rock major-element geochemical signature but with mineralogical and trace element characteristics of the alkaline magmas.

Further evidence to support this mixing hypothesis comes directly from the mineral compositions and textures. Core compositions in clinopyroxene and olivine phenocrysts within the Group II tephra are typically more magnesian than in the Group I tephra samples (Table 7), suggesting initial crystallization in a more mafic melt, whereas rim compositions are similar to those in the Group I tephra, indicating final equilibrium in similar melt compositions. Large step changes in Mg# in growth zones in clinopyroxene phenocrysts in both Group I and Group II tephra are coincident with equivalent changes in Cr_2O_3, indicating compositional changes as a result of magma mingling (Streck, 2008). Similar compositional changes are observed in the Group I orthopyroxene phenocrysts (Fig. 13). Plagioclase phenocrysts in both groups also display large compositional changes coincident with dissolution and resorption surfaces (Fig. 10). These changes in An content are commonly associated with Fe_2O_3, suggesting compositional changes in the melt as a result of magma mingling (Ginibre *et al.*, 2002*a*, 2002*b*).

Geochemical variations within the Group II units

The Group II units, N, F and D, display marked compositional variations with some samples showing whole-rock major and trace element concentrations and $^{87}Sr/^{86}Sr$ and $^{143}Nd/^{144}Nd$ ratios more akin to the Group I tephras (Figs 4–9). These geochemical variations could be the result of these samples being misinterpreted as belonging to units N, F and D. The samples are from different localities across the CVC, and difficulties in correlating the older, less well-exposed deposits could result in this misclassification. However, based on radiocarbon ages of binding ash horizons, stratigraphic correlations and field characteristics, we believe that these samples do belong to the Group II units N, F and D. Samples VF00-06Ps, VF95-01B and VF95-01C were collected from phlogopite-bearing scoria fall deposits. Sample VF10-04F (of unit F) was collected from a scoria fall deposit underlying an ash horizon that was dated at 11 840 ± 70 a BP corresponding to an eruption age for unit F of *c.* 12 000 a BP. Similarly, sample VF97-20D was collected from a scoria fall deposit directly overlying an ash horizon from which a charcoal sample yielded an age of 13 350 ± 130 a BP, coinciding with an eruption age of unit D of *c.* 13 000 a BP. Sample VF97-03BJ was collected from a well-dated section; charcoal from an overlying ash layer yielded an age of 6840 ± 80 a BP and charcoal from an underlying ash layer yielded an age of 7190 ± 90 a BP (Luhr *et al.*, 2010) giving an estimated age for this deposit of *c.* 7000 a BP coinciding with unit N. However, the dated ash layers bind three scoria fall and two ash deposits; therefore there is a degree of uncertainty in the correlation of this unit.

Based on the geochemical and mineralogical evidence of mixing between subalkaline and alkaline magmas, a plausible explanation for the geochemical distinctions revealed within the Group II units is that the more enriched samples represent more alkaline components of a mingled magma, whereas the more depleted samples represent the subalkaline end-member. Physical mixing between the two magma types within the crustal magma storage region of the CVC magmatic system could result in a mingled magma being erupted from the principal CVC vent, resulting in tephra fallout with some high-K, more alkaline clasts, and some geochemically more subalkaline clasts. Unit N displays less internal variation than units F and D, potentially reflecting a more well-mixed magma. This is consistent with the mineralogical data, as unit N has a mineral assemblage more similar to the Group I tephra than to units D and F.

Magma storage and shallower crustal processes

Although the CVC has been the focus of numerous petrological and geochemical studies (e.g. Luhr & Carmichael, 1980, 1990*b*; Medina-Martínez, 1983; Robin *et al.*, 1987, 1991; De la Cruz-Reyna, 1993; Luhr, 1993, 2002; Robin & Potrel, 1993; Righter, 2000; Navarro-Ochoa *et al.*, 2002; Saucedo *et al.*, 2005, 2010; Atlas *et al.*, 2006; Luhr *et al.*, 2006; Valdez-Moreno *et al.*, 2006; Reubi & Blundy, 2008; Savov *et al.*, 2008), very few have attempted to define the nature of the magmatic plumbing system beneath the CVC. Based on the water content of melt inclusions in plagioclase, pyroxene and hornblende phenocrysts within Colima lavas, Atlas *et al.* (2006) proposed that these melt

inclusions were trapped at depths of <12 km, and that entrapment continued throughout the period of magma ascent. Those researchers showed that water contents in the melt inclusions vary negatively with SiO_2 and K_2O; therefore, they concluded that plagioclase crystallization must have occurred during degassing under vapour-saturated conditions. Based on the lack of erupted rhyolitic magmas at the CVC, Atlas *et al.* (2006) suggested that evolved, degassed magmas stagnate in sills, and are remobilized by more mafic, less degassed magmas rising towards the surface. Atlas *et al.* (2006) therefore concluded that the CVC magmas evolved in conduits or inter-fingered dykes in the upper crust, rather than in a large stratified magma chamber.

Reubi & Blundy (2008) also studied melt inclusions in plagioclase, orthopyroxene and clinopyroxene phenocrysts in andesitic lavas from Volcán de Colima, which erupted between 1998 and 2005. They discarded the concept of a shallow magma chamber beneath the CVC, proposing instead lower crustal evolution of the Colima magmas rather than melt evolution in the upper crust, as proposed by Atlas *et al.* (2006). Their model is similar to the hot zone model of Annen *et al.* (2006), in which gabbroic sills are emplaced in the lower crust where the magma evolves through differentiation and crustal assimilation. Reubi & Blundy (2008) concluded that the Colima andesites formed through the incorporation of mafic gabbroic clots into evolved dacitic melts.

The above model requires further testing, as there are many aphyric and crystal-poor andesites erupted in volcanic arcs, including the CVC. In addition, whole-rock major and trace element (REE, HFSE) and radiogenic isotope (Sr, Nd, Pb) compositions of CVC andesites show remarkable similarities (this study; Valdez-Moreno *et al.*, 2006; Savov *et al.*, 2008; Luhr *et al.*, 2010; Verma & Luhr, 2010) over multiple eruptions; these are hard to explain by physical magma mixing (with exactly the same proportions) at shallow depths. Furthermore, the Reubi & Blundy (2008) model is based on a lack of intermediate glass compositions in Colima andesites. In contradiction to this, we have found that the medium-K subalkaline basaltic andesite (Group I) tephra samples from our study have mafic to felsic (54·1–75·8 wt % SiO_2; $n = 343$; Fig. 14e; Table 7) groundmass glass compositions, with the majority of analyses comprising intermediate compositions from 56 to 65 wt % SiO_2 ($n = 228$ from 30 samples).

Insights from mineral chemistry and textural characteristics

The complex zoning patterns observed in the plagioclase, clinopyroxene and orthopyroxene phenocrysts and microphenocrysts imply a complex crystallization history, involving multiple phases of growth and continually changing conditions (pressure, temperature, H_2O content, fO_2, and melt composition) within the magmatic plumbing system. Such changes in conditions can be a result of local magma mixing owing to convective overturn in a magma chamber, mafic magma recharge or depressurization under water-undersaturated conditions (Nelson & Montana, 1992; Blundy & Cashman, 2001; Ginibre *et al.*, 2002*a*, 2002*b*; Annen *et al.*, 2006; Ginibre & Wörner, 2007; Streck, 2008). The presence of multiple types of zoning and morphologies within a single eruption deposit can be attributed to crystal growth at different times and in different parts of the magmatic plumbing system; that is, early, deep crystallization versus late, shallow crystallization.

Strong disequilibrium textures, such as sieve textures, patchy zoned phenocrysts and cores, and dissolution surfaces, indicate repeated destabilization of phenocrysts during crystallization. The rounded and irregular rims displayed by sieve-textured plagioclase phenocrysts (Fig. 10a) indicate that the minerals were not in equilibrium with the final melt composition. Sieve textures can be the result of rapid crystal growth that forms boxy-like cellular, regular patterns (Streck, 2008); however, in this case the patchy zonation is irregular and displays cross-cutting relationships, suggesting that the phenocrysts have undergone pervasive resorption and recrystallization (Ginibre & Wörner, 2007). The crystal morphology reveals that the more sodic plagioclase is the original mineral composition, which underwent dissolution, followed by precipitation of a more calcic composition infilling holes in the original crystal. Pervasive resorption can result from temperature increase owing to mafic magma recharge, which, if mechanical mixing occurred, would cause growth of more calcic plagioclase (Ginibre & Wörner, 2007). Alternatively, it could result from depressurization under water-undersaturated conditions, which would destabilize the plagioclase causing dissolution, following which more calcic plagioclase would precipitate (Nelson & Montana, 1992; Ginibre & Wörner, 2007). If resorption and recrystallization resulted from mafic magma recharge, differences in anorthite content between the original and overgrown plagioclase would be expected to correlate with changes in other elements such as Fe and Mg (e.g. Smith *et al.*, 2009). However, in the sieve-textured plagioclase phenocrysts within the Group I and II tephra, there is no major difference in Fe and Mg content between the original more sodic, albite-rich plagioclase and the overgrown more anorthitic plagioclase, suggesting that this texture is not the result of magma mixing, but of depressurization.

Similar patchy sieve textures are also observed in growth zones in the clinopyroxene phenocrysts in the CVC tephra. Large-scale resorption and dissolution is commonly attributed to magma mixing; however, Crabtree & Lange (2011) showed that such textures can also result from large degrees of undercooling caused by degassing. At large undercoolings, crystal growth rates are higher, resulting in diffusion limited growth, producing crystals with skeletal, dendritic and hopper textures

(Humphreys *et al.*, 2006; Crabtree & Lange, 2011). Subsequent crystallization can form patchy textures and reverse or normal zoning. EPMA analyses together with back-scattered electron (BSE) images show that the strong resorption events with step increases in Mg# observed in clinopyroxene phenocrysts in the CVC tephra coincide with increases in Cr_2O_3 (Figs 11 and 12), indicating that these events are linked to destabilization and recrystallization in a more mafic melt (Streck, 2008). Conversely, resorption events with step decreases in Mg# and coinciding decreases in Cr_2O_3, as observed between the dark, high-Mg zone, and the low-Mg growth to the rim (Figs 11b and 12a), indicate resorption and re-equilibration in a more evolved melt. Small-scale oscillations in Mg#, but not Cr, in the outer growth zone (Figs 11a and 12a) could indicate fluctuations in pressure, temperature, volatile content and fO_2 (Streck, 2008). Embayed crystal edges indicate that the clinopyroxene phenocrysts were not in equilibrium with the final melt composition (Streck, 2008).

Figure 18 is a schematic representation of the CVC magmatic plumbing system based on the interpretation of the petrological data presented here. A shallow-level magma storage region is indicated by the presence of plagioclase phenocrysts with small-scale oscillatory zoning and embayed rims, which suggest thermal convection in a magma chamber (Ginibre *et al.*, 2002*a*; Ginibre & Wörner, 2007). The presence of amphibole phenocrysts with breakdown rims is indicative of water loss, owing to slow magma ascent rates allowing time for sufficient degassing, as observed in Colima lava and dome samples (Valdez-Moreno *et al.*, 2006; Savov *et al.*, 2008), and/or to long residence times in a shallow magma chamber (Browne & Gardner, 2006; Rutherford, 2008).

Rapid ascent rates from the magma storage region for the CVC explosive eruption deposits are revealed by the highly vesiculated nature of the groundmass and the occurrence of hornblende phenocrysts with stable, sharp crystal edges, much like those in the highly explosive 1913 tephra (Luhr *et al.*, 2006). The presence of amphibole phenocrysts with breakdown rims is therefore attributed to their long residence times in a shallow-level magma storage region. The majority of scoria and pumice samples from the CVC tephra fallout deposits studied here exhibit both stable and unstable amphibole phenocrysts. The observed juxtaposition of stable and unstable amphibole phenocrysts within the same thin section implies late-stage magma mixing events (Rutherford, 2008), which may have triggered the explosive eruptions (e.g. Pallister *et al.*, 1992).

Magma mixing or mingling in the magmatic plumbing system of the CVC is also revealed by the nature of the 1913 eruption and its deposits (Robin & Potrel, 1993; Luhr, 2002; Luhr *et al.*, 2006, 2010; Saucedo *et al.*, 2010; Reubi *et al.*, 2014). The more mafic nature of the 1818 and the 1913 eruptions compared with pre- and post-1913 lavas led Luhr (2002) to conclude that the proposed 100 year eruption cycle of explosive activity at Volcán de Colima terminates with the injection of a hot, mafic magma that is deep in origin and is capable of triggering an explosive Plinian eruption (e.g. Pallister *et al.*, 1996).

The explosive CVC eruption deposits reveal the presence of a complex magmatic plumbing system beneath the CVC, involving multiple magma storage levels from the base of the crust to a shallow-level upper crustal magma storage region (Fig. 18). This is supported by recent geophysical studies, which have imaged two potential magma storage regions beneath Volcán de Colima at ~5 km and 15-30 km depth (Gardine, 2010; López-Loera, 2012).

High-K magmas as a trigger of Plinian eruptions

The appearance of the distinct mafic high-K Group II eruption deposits within the medium-K subalkaline stratigraphy suggests that pulses of alkaline magma periodically intercept and become incorporated into the magmatic plumbing system of the CVC. These primitive magmas could potentially trigger the explosive eruption of CVC magmas. Scoria from the 1913 Plinian eruption of Volcán de Colima is streaky, showing evidence of magma mingling (Robin & Potrel, 1993; Luhr, 2002; Luhr *et al.*, 2006, 2010; Saucedo *et al.*, 2010; Reubi *et al.*, 2014). The majority of the CVC pumices and scoria are streaky with large variations in groundmass glass composition (Fig. 14e). This, together with the petrological evidence of magma mingling revealed by mineral chemistry and zoning patterns, indicates that magma mingling is a dominant process at the CVC. Similar processes are observed in arc volcanoes worldwide. For example, recent studies of lavas and pyroclastic deposits from the Old and Young Shiveluch Volcanoes in Kamchatka have suggested that the input of primitive magma into the lower levels of the magma chamber triggers explosive Plinian eruptions (Gorbach & Portnyagin, 2011; Gorbach *et al.*, 2013). Shiveluch is a dominantly andesitic stratovolcano characterized by explosive Plinian eruptions and lava dome growth. Similar to the CVC, interbedded within the dominantly intermediate eruption deposits are the products of single mafic eruptions (Gorbach & Portnyagin, 2011). It is these that have been linked to small injections of more primitive magma at depth. Older eruptions dated at 3600 and 7600 ^{14}C a BP are of potassic basalt and basaltic andesite, respectively. Gorbach & Portnyagin (2011) suggested that these eruptions, and those older than *c.* 10 000 a BP, were related to more active replenishment of the magma chamber system by deep magma inputs.

The appearance of primitive, high-K magmas at predominantly intermediate to felsic arc volcanoes is not unique to the CVC and Kamchatka. Primitive magmas

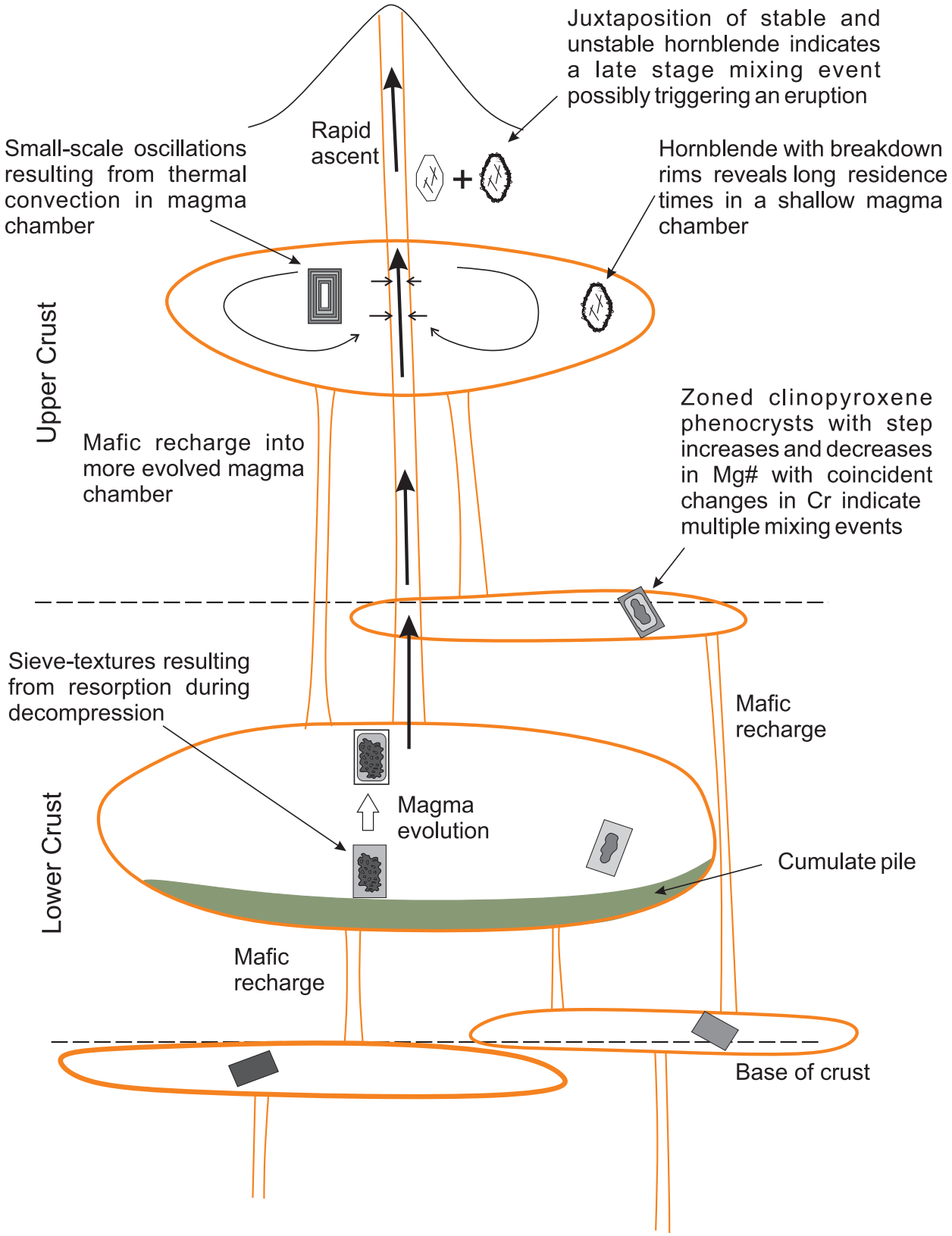

Fig. 18. Schematic representation of the magmatic plumbing system of the CVC based on the interpretation of the petrological data and geophysical data (Gardine, 2010; López-Loera, 2012).

have erupted in monogenetic cones alongside more evolved arc volcanoes, for example, in the Izu–Bonin–Marianas arc (shoshonite volcanic province: see Stern *et al.*, 2003, and references therein), the Sunda–Banda Arc, Indonesia (Wheller *et al.*, 1987; Macpherson *et al.*, 2010), the Cascades, and along the TMVB (e.g. Hasenaka & Carmichael, 1985; Lange & Carmichael, 1990, 1991; Hasenaka *et al.*, 1994; Carmichael *et al.*, 1996; Gómez-Tuena *et al.*, 2003, 2007; Straub *et al.*, 2013; Díaz-Bravo *et al.*, 2014). The presence of high-K tephra layers that show clear geochemical and petrological evidence for physical magma mingling between medium-K, subalkaline and shoshonitic alkaline magmas within the predominantly medium-K subalkaline CVC eruptive stratigraphy reveals a link between these two distinct magma types. This magma mingling process may be a common occurrence in volcanic arc settings, which the well-preserved eruptive stratigraphy of the CVC provides a means to explore further.

The evolution of the CVC stratovolcanoes has been governed by large sector-collapse events producing debris avalanche deposits to the SE, south and SW of the CVC (Robin *et al.*, 1987; Luhr & Prestegaard, 1988; Luhr & Carmichael, 1990*a*; Stoopes & Sheridan, 1992; Komorowski *et al.*, 1997; Cortés *et al.*, 2009; Norini *et al.*, 2010). The five most recent debris-avalanche deposits have been dated through radiocarbon techniques and yielded ages of 2550 ± 110, 3600 ± 120, 7040 ± 160, 9671 ± 88 and 18 520 ± 260 a BP (Stoopes & Sheridan, 1992; Komorowski *et al.*, 1997; Cortés *et al.*, 2009). There appears to be no clear temporal link between these large collapse events and the high-K mafic magma pulses that erupted at *c.* 7000, *c.* 12 000 and *c.* 13 000 a BP. However, there may have been more, deeper injections of mafic, high-K magma that have not been preserved in the stratigraphic record, or were low in volume, but that nevertheless induced instabilities such as higher temperatures and high volatile contents, which may have been the trigger for such large sector-collapse events. Further investigations into the links between mafic magma injections and large sector-collapse events at Volcán de Colima may provide an analogue for subalkaline caldera systems such as Santorini (Druitt & Francaviglia, 1992) or Long Valley Caldera, California (Hildreth, 2004), where long-term tephra records are not preserved.

SUMMARY AND CONCLUSIONS

Field, geochemical and petrological investigations of the tephra fallout deposits of Volcán de Colima have revealed the presence of three distinct high-K mafic scoria fall deposits (Group II) that have characteristics intermediate between those of the medium-K subalkaline basaltic andesite and andesite tephra deposits (Group I) with which they are interbedded, and alkaline mafic magmas similar to those that formed monogenetic cinder cones on the Colima rift floor. These high-K mafic magmas represent mixtures between subalkaline and alkaline magmas, with up to 50% of the alkaline magma component.

Evidence from the mineral compositions and zoning patterns of phenocrysts within the CVC Group I and Group II eruption deposits reveals multiple magma mixing events in the magmatic plumbing system. Group II tephra contain phenocrysts that are also observed in the Group I samples, revealing a shared provenance. This suggests physical mixing between the alkaline and subalkaline magmas, and that the Group II high-K mafic magmas are evolving within the subalkaline magma storage region beneath the CVC. This study reveals that the magmatic plumbing system of the CVC is an open system with common magma mingling and mixing events, and that the alkaline and subalkaline activity is inter-related. This may well be the case in many other arc settings where both alkaline and subalkaline magmas are erupted; that is, the Izu–Bonin–Mariana arc (shoshonite volcanic province: see Stern *et al.*, 2003, and references therein), the Sunda–Banda Arc, Indonesia (Wheller *et al.*, 1987) and central Kamchatka (Koloskov *et al.*, 1999).

The presence of the high-K mafic scoria fall deposits within the dominantly medium-K subalkaline tephra record at ~7000, 12 000 and 13 000 a BP indicates that pulses of alkaline mafic magmas rise and periodically intercept the well-established magmatic plumbing system of the CVC on timescales of a few thousand years and may contribute to the onset of highly explosive Plinian eruptions. Future petrological and geochemical monitoring of the near-terminal (post-1913) 100 year CVC cycle should be able to detect the arrival of even low volumes of alkaline, mafic, hot, volatile-rich magma into the CVC conduit. These are magma properties that are not easily recognized by geophysical monitoring techniques, but deserve the full attention of the local civil protection authorities and the monitoring community as potentially unique tracers of future highly explosive eruptions.

ACKNOWLEDGEMENTS

We would like to dedicate our work to the living memory of the pioneers of the studies of petrology and geochemistry of the Colima Volcanic Complex—Jim Luhr and Ian Carmichael. Our studies benefited greatly from the support of staff from the Colima Volcano Observatory (CVO). We are particularly grateful for the logistical field support provided by the director of the CVO, Gabriel Reyes. We would like to thank Eric Condliffe and Richard Walshaw for help with SEM and EPMA analyses, and Susan Loughlin for fruitful discussions. We thank the curators of the Mineralogy and Petrology Collections of the Department of Mineral Sciences at the National Museum of Natural History (Smithsonian Institution) in

Washington DC, USA, for lending us samples and thin sections from Jim Luhr's Colima collection. This paper is published with permission of the Executive Director of the British Geological Survey (Natural Environment Research Council).

FUNDING

This work was funded through a Natural Environmental Research Council studentship held by J.M.C. at the University of Leeds and supported by the British Geological Survey Funding Initiative (BUFI).

SUPPLEMENTARY DATA

Supplementary data are available at *Journal of Petrology* online.

REFERENCES

Allan, J. (1986). Geology of the Colima and Zacoalco grabens, SW Mexico: Late Cenozoic rifting in the Mexican Volcanic Belt. *Geological Society of America Bulletin* **97**, 473–485.

Allan, J. F. & Carmichael, I. S. E. (1984). Lamprophyric lavas in the Colima graben, SW Mexico. *Contributions to Mineralogy and Petrology* **88**, 203–216.

Annen, C., Blundy, J. D. & Sparks, R. S. J. (2006). The genesis of intermediate and silicic magmas in deep crustal hot zones. *Journal of Petrology* **47**, 505–539.

Atlas, Z. D., Dixon, J. E., Sen, G., Finny, M. & Martin-Del Pozzo, A. L. (2006). Melt inclusions from Volcan Popocatepetl and Volcan de Colima, Mexico: Melt evolution due to vapor-saturated crystallization during ascent. *Journal of Volcanology and Geothermal Research* **153**, 221–240.

Bebout, G. E. & Barton, M. D. (1989). Fluid-flow and metasomatism in a subduction zone hydrothermal system: Catalina Schist Terrane, California. *Geology* **17**, 976–980.

Blundy, J. & Cashman, K. (2001). Ascent-driven crystallisation of dacite magmas at Mount St Helens, 1980–1986. *Contributions to Mineralogy and Petrology* **140**, 631–650.

Bretón González, M., Ramírez, J. J. & Navarro-Ochoa, C. (2002). Summary of the historical eruptive activity of Volcan de Colima, México, 1519–2000. *Journal of Volcanology and Geothermal Research* **117**, 21–46.

Browne, B. L. & Gardner, J. E. (2006). The influence of magma ascent path on the texture, mineralogy, and formation of hornblende reaction rims. *Earth and Planetary Science Letters* **246**, 161–176.

Cai, Y. (2009). Tracing upper mantle heterogeneities with radiogenic isotopes at the Mexican Volcanic Belt and the Arctic Gakkel Ridge, PhD thesis, Columbia University, New York.

Carmichael, I., Lange, R. & Luhr, J. F. (1996). Quaternary minettes and associated volcanic rocks of Mascota, western Mexico: a consequence of plate extension above a subduction modified mantle wedge. *Contributions to Mineralogy and Petrology* **124**, 302–333.

Carmichael, I., Frey, H., Lange, R. & Hall, C. (2006). The Pleistocene cinder cones surrounding Volcán Colima, Mexico re-visited: eruption ages and volumes, oxidation states, and sulfur content. *Bulletin of Volcanology* **68**, 407–419.

Cortés, A., Garduño, V. H., Navarro-Ochoa, C., Komorowski, J. C., Saucedo, R., Macías, J. L. & Gavilanes, J. C. (2005). *Carta Geológica del Complejo Volcánico de Colima, con Geología del Complejo Volcánico de Colima. Universidad Nacional Autónoma de México, Instituto de Geología, Cartas Geológicas y Mineras* **10**.

Cortés, A., Macías, J. L., Capra, L. & Garduño-Monroy, V. H. (2009). Sector collapse of the SW flank of Volcán de Colima, México: The 3600 yr BP La Lumbre–Los Ganchos debris avalanche and associated debris flows. *Journal of Volcanology and Geothermal Research* **197**, 52–66.

Cortés, A., Garduño, V. H., Macías, J. L., Navarro-Ochoa, C., Komorowski, J. C., Saucedo, R. & Gavilanes, J. C. (2010). Geologic mapping of the Colima volcanic complex (Mexico) and implications for hazard assessment. In: Groppelli, G. & Viereck-Goette, L. (eds) *Stratigraphy and Geology of Volcanic Areas. Geological Society of America, Special Papers* **464**, 249–264.

Cox, K. G., Bell, J. D. & Pankhurst, R. J. (1979). *The Interpretation of Igneous Rocks*. Allen & Unwin.

Crabtree, S. M. & Lange, R. A. (2011). Complex phenocryst textures and zoning patterns in andesites and dacties: Evidence of degassing-induced rapid crystallisation? *Journal of Petrology* **52**, 3–38.

Crummy, J. M. (2013). Holocene evolution of the Colima Volcanic Complex, Mexico, PhD thesis, University of Leeds.

De la Cruz-Reyna, S. (1993). Random patterns of activity at Colima volcano, Mexico. *Journal of Volcanology and Geothermal Research* **55**, 51–68.

Díaz-Bravo, B. A., Gómez-Tuena, A., Ortega-Obregón, C. & Pérez-Arvizu, O. (2014). The origin of intraplate magmatism in the western Trans-Mexican Volcanic Belt. *Geosphere* GES00976.1.

Druitt, T. & Francaviglia, V. (1992). Caldera formation on Santorini and the physiography of the islands in the late Bronze Age. *Bulletin of Volcanology* **54**, 484–493.

Ferrari, L. (2004). Slab detachment control on mafic volcanic pulse and mantle heterogeneity in central Mexico. *Geology* **32**, 77–80.

Ferrari, L. & Rosas-Elguera, J. (2000). Late Miocene to Quaternary extension at the northern boundary of the Jalisco block, western Mexico: the Tepic–Zacoalca rift revisited. In: Aguirre-Diaz, G., Delgado-Granados, H. & Stock, J. (eds) *Cenozoic Tectonics and Volcanism of Mexico. Geological Society of America, Special Papers* **334**, 42–64.

Ferrari, L., Petrone, C. M. & Francalanci, L. (2001). Generation of ocean-island basalt-type volcanism in the western Trans-Mexican volcanic belt by slab rollback, asthenosphere infiltration, and variable flux melting. *Geology* **29**, 507–510.

Ferrari, L., Orozco-Esquivel, T., Manea, V. & Manea, M. (2012). The dynamic history of the Trans-Mexican Volcanic Belt and the Mexico subduction zone. *Tectonophysics* **522**, 122–149.

Gardine, M. D. (2010). Tracing the movement and storage of magma in the crust through seismology: Examples from Alaska and western Mexico, PhD thesis, University of Alaska Fairbanks.

Garduño, V. H., Saucedo, R., Jimenez, S., Gavilanes, J. C., Cortes, A. & Uribe, R. M. (1998). La Falla Tamazula, limite suroriental del bloque Jalisco, y sus relaciones cone el Complejo Volcanico de Colima, Mexico. *Revista Mexicana de Ciencias Geologicas* **15**, 132–144.

Ginibre, C. & Wörner, G. (2007). Variable parent magmas and recharge regimes of the Parinacota magma system (N. Chile) revealed by Fe, Mg and Sr zoning in plagioclase. *Lithos* **98**, 118–140.

Ginibre, C., Kronz, A. & Wörner, G. (2002*a*). High-resolution quantitative imaging of plagioclase composition using accumulated backscattered electron images: new constraints on oscillatory zoning. *Contributions to Mineralogy and Petrology* **142**, 436–448.

Ginibre, C., Wörner, G. & Kronz, A. (2002*b*). Minor- and trace-element zoning in plagioclase: implications for magma chamber processes at Parinacota volcano, northern Chile. *Contributions to Mineralogy and Petrology* **143**, 300–315.

Gómez-Tuena, A., Orozco-Esquivel, M. T. & Ferrari, L. (2007). *Igneous petrogenesis of the Trans-Mexican volcanic belt: Geological Society of America Special Papers* **422**, 129–181.

Gómez-Tuena, A., LaGatta, A., Langmuir, C. H., Goldstein, S. L., Ortega-Gutiérrez, F. & Carrasco-Nuñez, G. (2003). Temporal control of subduction magmatism in the eastern Trans-Mexican Volcanic Belt: mantle sources, slab contributions and crustal contamination. *Geochemistry, Geophysics, Geosystems* **4**, 8912.

Gorbach, N. & Portnyagin, M. V. (2011). Geology and petrology of the lava complex of Young Shiveluch Volcano, Kamchatka. *Petrology* **19**, 134–166.

Gorbach, N., Portnyagin, M. & Tembrel, I. (2013). Volcanic structure and composition of Old Shiveluch volcano, Kamchatka. *Journal of Volcanology and Geothermal Research* **263**, 193–208.

Halama, R., Savov, I., Rudnick, R. & McDonough, W. (2009). Insights into Li and Li isotope cycling and sub-arc metasomatism from veined mantle xenoliths, Kamchatka. *Contributions to Mineralogy and Petrology* **158**, 197–222.

Hasenaka, T. & Carmichael, I. S. (1985). The cinder cones of Michoacán–Guanajuato, central Mexico: their age, volume and distribution, and magma discharge rate. *Journal of Volcanology and Geothermal Research* **25**, 105–124.

Hasenaka, T., Ban, M. & Delgado-Granados, H. (1994). Contrasting volcanism in the Michoacán–Guanajuato volcanic field, central Mexico: Shield volcanoes vs. cinder cones. *Geofisica Internacional* **33**, 125–138.

Hildreth, W. (2004). Volcanological perspectives on Long Valley, Mammoth Mountain, and Mono Craters: several contiguous but discrete systems. *Journal of Volcanology and Geothermal Research* **136**, 169–198.

Humphreys, M. C. S., Blundy, J. D. & Sparks, R. S. J. (2006). Magma evolution and open-system processes at Shiveluch volcano: Insights from phenocryst zoning. *Journal of Petrology* **47**, 2303–2334.

Koloskov, A., Flerov, G., Seliverstov, V., Dorendorf, F. & Churikova, T. (1999). Potassic volcanics of central Kamchatka and the Late Cretaceous–Paleogene Kuril–Kamchatka alkaline province. *Petrologiya* **7**, 527–543.

Komorowski, J. C., Navarro, C., Cortés, A., Saucedo, R., Gavilanes, J. C., Siebe, C., Espindola, J.M. & Rodriguez, S. (1997). The Colima Volcanic Complex, part I: Quaternary multiple debris-avalanche deposits, part II: historical pyroclastic sequences (1913, 1991, 1994) In *IAVCEI (International Association of Volcanology and Chemistry of the Earth s Interior) General Assembly, Pre-Conference Excursion Guide* **3**.

Lange, R. A. & Carmichael, I. S. E. (1990). Hydrous basaltic andesites associated with minette and related lavas in western Mexico. *Journal of Petrology* **31**, 1225–1259.

Lange, R. A. & Carmichael, I. S. (1991). A potassic volcanic front in western Mexico: The lamprophyric and related lavas of San Sebastian. *Geological Society of America Bulletin* **103**, 928–940.

Langmuir, C. H., Vocke, R. D., Jr, Hanson, G. N. & Hart, S. R. (1978). A general mixing equation with applications to Icelandic basalts. *Earth and Planetary Science Letters* **37**, 380–392.

Leake, B. E., Woolley, A. R., Arps, C. E. S. *et al.* (1997). Nomenclature of amphiboles: Report of the subcommittee on amphiboles of the International Mineralogical Association, commission on new minerals and mineral names. *Canadian Mineralogist* **35**, 219–246.

Le Maitre, R. W., Streckeisen, A., Zanettin, B., Le Bas, M. J., Bonin, B., Bateman, P., Bellieni, G., Dudek, A., Efremova, S., Keller, J., Lameyre, J., Sabine, P. A., Schmid, R., Sorenson, H. & Wooley, A. R. (2002). *Igneous Rocks A Classification and Glossary of Terms*. Cambridge University Press.

López-Loera, H. (2012). 2 3/4 dimension modelling of the aeromagnetic anomaly of Volcán de Colima, western Mexico. *Geofisica Internacional* **51**, 129–142.

Luhr, J. F. (1993). Petrology and geochemistry of stage-I andesites and dacites from the caldera wall of Volcán Colima, Mexico. *Geofisica Internacional* **32**, 591–603.

Luhr, J. F. (2002). Petrology and geochemistry of the 1991 and 1998–1999 lava flows from Volcán de Colima, Mexico: implications for the end of the current eruptive cycle. *Journal of Volcanology and Geothermal Research* **117**, 169–194.

Luhr, J. F. & Carmichael, I. S. E. (1980). The Colima Volcanic Complex, Mexico: Part I. Post-caldera andesites from Volcán Colima. *Contributions to Mineralogy and Petrology* **71**, 343–372.

Luhr, J. F. & Carmichael, I. S. E. (1981). The Colima Volcanic Complex, Mexico: Part II. Late-Quaternary cinder cones. *Contributions to Mineralogy and Petrology* **76**, 127–147.

Luhr, J. F. & Carmichael, I. S. E. (1982). The Colima Volcanic Complex, Mexico: Part III. Ash and scoria fall deposits from upper slopes of Volcán Colima. *Contributions to Mineralogy and Petrology* **42**, 235–260.

Luhr, J. & Carmichael, I. E. (1985). Jorullo Volcano, Michoacan, Mexico (1759–1774): The earliest stages of fractionation in calc-alkaline magmas. *Contributions to Mineralogy and Petrology* **90**, 142–161.

Luhr, J. F. & Carmichael, I. S. E. (1990*a*). *Geology of Volcán de Colima*. Mexico City: Universidad Nacional Autónoma de México, Instituto de Geología.

Luhr, J. F. & Carmichael, I. S. E. (1990*b*). Petrological monitoring of cyclical eruptive activity at Volcán de Colima, Mexico. *Journal of Volcanology and Geothermal Research* **42**, 235–260.

Luhr, J. F. & Prestegaard, K. L. (1988). Caldera formation at Volcán Colima, Mexico, by a large Holocene volcanic debris avalanche. *Journal of Volcanology and Geothermal Research* **35**, 335–348.

Luhr, J. F., Navarro-Ochoa, C., Connor, C. B. & Connor, L. (2006). The 1913 VEI-4 Plinian eruption of Volcan de Colima (Mexico): tephrochronology, petrology and plume modelling. *EOS Transactions, American Geophysical Union* **52**, 1786.

Luhr, J. F., Navarro-Ochoa, C. & Savov, I. P. (2010). Tephrochronology, petrology and geochemistry of Late-Holocene pyroclastic deposits from Volcán de Colima, Mexico. *Journal of Volcanology and Geothermal Research* **197**, 1–32.

Macpherson, C. G., Chiang, K. K., Hall, R., Nowell, G. M., Castillo, P. R. & Thirlwall, M. F. (2010). Plio-Pleistocene intra-plate magmatism from the southern Sulu Arc, Semporna peninsula, Sabah, Borneo: Implications for high-Nb basalt in subduction zones. *Journal of Volcanology and Geothermal Research* **190**, 25–38.

Maria, A. H. & Luhr, J. F. (2008). Lamprophyres, basanites, and basalts of the western Mexican volcanic belt: Volatile contents and a vein–wallrock melting relationship. *Journal of Petrology* **49**, 2123–2156.

McInnes, B. I. A., Gregoire, M., Binns, R. A., Herzig, P. M. & Hannington, M. D. (2001). Hydrous metasomatism of oceanic subarc mantle, Lihir, Papua New Guinea: petrology and geochemistry of fluid-metasomatised mantle wedge xenoliths. *Earth and Planetary Science Letters* **188**, 169–183.

Medina-Martínez, F. (1983). Analysis of the eruptive history of the Volcán de Colima, México (1560–1980). *Geofísica Internacional* **22**, 157–178.

Navarro-Ochoa, C., Gavilanes, J. C. & Cortés, A. (2002). Movement and emplacement of lava flows at Volcán de Colima, México: Nov. 1998–Feb. 1999. *Journal of Volcanology and Geothermal Research* **117**, 155–167.

Nelson, S. T. & Montana, A. (1992). Sieve-textured plagioclases in volcanic rocks produced by rapid decompression. *American Mineralogist* **77**, 1242–1249.

Norini, G., Capra, L., Groppelli, G., Agliardi, F., Pola, A. & Cortes, A. (2010). Structural architecture of the Colima Volcanic Complex. *Journal of Geophysical Research* **115**, B12209.

Pallister, J. S., Hoblitt, R. P. & Reyes, A. G. (1992). A basalt trigger for the 1991 eruptions of Pinatubo volcano? *Nature* **356**, 426–428.

Pallister, J. S., Hoblitt, R. P., Meeker, G. P., Knight, R. J. & Siems, D. F. (1996). Magma mixing at Mount Pinatubo: Petrographic and chemical evidence from the 1991 deposits. In: Newhall, C. G. & Punongbayan, R. S. (eds) *Fire and Mud: Eruptions and Lahars of Mount Pinatubo, Philippines*. Philippine Institute of Volcanology and Seismology/University of Washington Press, pp. 687–731.

Pearce, J. A. (1982). Trace element characteristics of lavas from destructive plate boundaries. In: Thorpe, R. S. (ed.) *Andesites: Orogenic Andesites and Related Rocks*. John Wiley, pp. 525–548.

Reubi, O. & Blundy, J. (2008). Assimilation of plutonic roots, formation of high-K exotic melt inclusions and genesis of andesitic magmas at Volcán De Colima, Mexico. *Journal of Petrology* **49**, 2221–2243.

Reubi, O., Blundy, J. & Pickles, J. (2014). Petrological monitoring of Volcan de Colima magmatic system: the 1998 to 2010 activity. In: Varley, N. R. & Komorowski, J. C. (eds) *Volcan de Colima: Managing the Threat*. Springer (in press).

Righter, K. (2000). A comparison of basaltic volcanism in the Cascades and western Mexico: compositional diversity in continental arcs. *Tectonophysics* **318**, 99–117.

Robin, C. & Potrel, A. (1993). Multi-stage magma mixing in the precaldera series of Fuego de Colima volcano. *Geofisica Internacional* **32**, 605–615.

Robin, C., Mossand, P., Camus, G., Cantagrel, J. M., Gourgaud, A. & Vincent, P. M. (1987). Eruptive history of the Colima Volcanic Complex (Mexico). *Journal of Volcanology and Geothermal Research* **31**, 99–113.

Robin, C., Camus, G. & Gourgaud, A. (1991). Eruptive and magmatic cycles at Fuego de Colima volcano (Mexico). *Journal of Volcanology and Geothermal Research* **45**, 209–225.

Rutherford, M. J. (2008). Magma ascent rates. In: Putirka, K. D. & Tepley, F. J., III (eds) *Minerals, Inclusions and Volcanic Processes. Mineralogical Society of America and Geochemical Society, Reviews in Mineralogy and Geochemistry* **69**, 241–271.

Saucedo, R., Macias, J. L., Sheridan, M. F., Bursik, M. I. & Komorowski, J. C. (2005). Modeling of pyroclastic flows of Colima Volcano, Mexico: implications for hazard assessment. *Journal of Volcanology and Geothermal Research* **139**, 103–115.

Saucedo, R., Macias, J. L., Gavilanes, J. C., Arce, J. L., Komorowski, J. C., Gardner, J. E. & Valdez-Moreno, G. (2010). Eyewitness, stratigraphy, chemistry, and eruptive dynamics of the 1913 Plinian eruption of Volcan de Colima, Mexico. *Journal of Volcanology and Geothermal Research* **191**, 149–166.

Saunders, A. D., Norry, M. J. & Tarney, J. (1991). Fluid influence on the trace element compositions of subduction zone magmas. *Philosophical Transactions of the Royal Society of London, Series A* **335**, 377–392.

Savov, I. P., Luhr, J. F. & Navarro-Ochoa, C. (2008). Petrology and geochemistry of lava and ash erupted from Volcán Colima, Mexico, during 1998–2005. *Journal of Volcanology and Geothermal Research* **174**, 241–256.

Savov, I. P., Ryan, J. G., D'Antonio, M. & Fryer, P. (2007). Shallow slab fluid release across and along the Mariana arc–basin system: Insights from geochemistry of serpentinized peridotites from the Mariana fore arc. *Journal of Geophysical Research* **112**, B09205.

Schmidt, M. E. & Grunder, A. L. (2011). Deep mafic roots to arc volcanoes: Mafic recharge and differentiation of basaltic andesite at North Sister Volcano, Oregon Cascades. *Journal of Petrology* **52**, 306–341.

Smith, V. C., Blundy, J. D. & Arce, J. L. (2009). A Temporal Record of Magma Accumulation and Evolution beneath Nevado de Toluca, Mexico, Preserved in Plagioclase Phenocrysts. *Journal of Petrology* **50**, 405–426.

Soto, G. L., Ni, J. F., Grand, S. P., Sandvol, E., Valenzuela, R. W., Speziale, M. G., Gonzalez, J. M. G. & Reyes, T. D. (2009). Mantle flow in the Rivera–Cocos subduction zone. *Geophysical Journal International* **179**, 1004–1012.

Stern, R. J., Fouch, M. J. & Klemperer, S. (2003). An overview of the Izu–Bonin–Mariana subduction factory. In: Eiler, J. & Hirschmann, M. (eds) *Inside the Subduction Factory. Geophysical Monograph, American Geophysical Union* **138**, 175–222.

Stoopes, G. R. & Sheridan, M. F. (1992). Giant debris avalanches from the Colima volcanic complex, Mexico: Implications for long-runout landslides (<100 km) and hazard assessment. *Geology* **20**, 299–302.

Straub, S. M., Goldstein, S. L., Class, C., Schmidt, A. & Gomez-Tuenca, A. (2010). Slab and mantle controls on the Sr–Nd–Pb–Hf isotope evolution of the post 42 Ma Izu–Bonin volcanic arc. *Journal of Petrology* **51**, 993–1026.

Straub, S. M., Gómez-Tuena, A., Zellmer, G. F., Espinasa-Perena, R., Stuart, F. M., Cai, Y., Langmuir, C. H., Martin-Del Pozzo, A. L. & Mesko, G. T. (2013). The processes of melt differentiation in arc volcanic rocks: Insights from OIB-type arc magmas in the central Mexican volcanic belt. *Journal of Petrology* **54**, 665–701.

Streck, M. J. (2008). mineral textures and zoning as evidence for open system processes. In: Putirka, K. D. & Tepley, F. J., III (eds) *Minerals, Inclusions and Volcanic Processes. Mineralogical Society of America and Geochemical Society, Reviews in Mineralogy and Geochemistry* **69**, 595–622.

Sun, S. S. & McDonough, W. F. (1989). Chemical and isotopic systematics of ocean basalts: implications for mantle composition and processes. In: Saunders, A. D. & Norry, M. J. (eds) *Magmatism in the Ocean Basins. Geological Society, London, Special Publications* **42**, 313–345.

Tatsumi, Y., Murasaki, M. & Nohda, S. (1992). Across-arc variation of lava chemistry in the Izu–Bonin Arc—identification of subduction components. *Journal of Volcanology and Geothermal Research* **49**, 179–190.

Thirlwall, M. F. (1991). Long-term reproducibility of multicollector Sr and Nd isotope ratio analysis. *Chemical Geology* **94**, 85–104.

Valdez-Moreno, G., Schaaf, P., Macias, J. L. & Kusakabe, M. (2006). New Sr–Nd–Pb–O isotope data for Colima Volcano and evidence for the nature of the local basement. In: Siebe, C., Macias, J. L. & Aguirre-Diaz, G. J. (eds) Neogene-Quaternary continental margin volcanism: A perspective from Mexico. *Geological Society of America, Special Papers* **334**, 1–28.

Varley, N., Arámbula-Mendoza, R., Reyes-Dávila, G., Stevenson, J. & Harwood, R. (2010). Long-period seismicity during magma movement at Volcán de Colima. *Bulletin of Volcanology* **72**, 1093–1107.

Verma, S. P. & Luhr, J. F. (2010). Sr, Nd, and Pb isotopic evidence for the origin and evolution of the Cántaro–Colima volcanic chain, Western Mexican Volcanic Belt. *Journal of Volcanology and Geothermal Research* **197**, 33–51.

Vigouroux, N., Wallace, P. J. & Kent, A. J. R. (2008). Volatiles in High-K magmas from the western Trans-Mexican Volcanic Belt: evidence for fluid fluxing and extreme enrichment of the mantle wedge by subduction processes. *Journal of Petrology* **49**, 1589–1618.

Wheller, G. E., Varne, R., Foden, J. D. & Abbott, M. J. (1987). Geochemistry of Quaternary volcanism in the Sunda–Banda arc, Indonesia, and three-component genesis of island-arc basaltic magmas. *Journal of Volcanology and Geothermal Research* **32**, 137–160.

Wilcox, R. E. (1954). Petrology of Paricutin Volcano, Mexico. *US Geological Survey Bulletin* **965C**, 281–353.

Yang, T., Grand, S. P., Wilson, D., Guzman-Speziale, M., Gomez-Gonzalez, J. M., Dominguez-Reyes, T. & Ni, J. (2009). Seismic structure beneath the Rivera subduction zone from finite-frequency seismic tomography. *Journal of Geophysical Research—Solid Earth* **114**, 1–12.

Zobin, V. M., Luhr, J. F., Taran, Y. A., Breton Gonzalez, M., Cortes, A., De la Cruz-Reyna, S., Dominguez-Reyes, T., Galindo, L., Gavilanes, J. C., Munez, J. J., Navarro-Ochoa, C., Ramirez, J. J., Reyes, G. A., Ursua, M., Velasco, J., Alatorre, E. & Satiago, H. (2002). Overview of the 1997–2000 activity of Volcan de Colima, Mexico. *Journal of Volcanology and Geothermal Research* **117**, 1–19.

Zobin, V. M., Varley, N. R., González, M., Orozco, J., Reyes, G. A., Navarro, C. & Bretón, M. (2008). Monitoring the 2004 andesitic block-lava extrusion at Volcan de Colima, Mexico from seismic activity and SO_2 emission. *Journal of Volcanology and Geothermal Research* **177**, 367–377.